energies

MDPI

Article

Adaptive Re-Clearing of Locational Marginal Electricity–Carbon Signals for Collective Demand Response in Urban Energy Systems

Jingwei Xue [1,*], Linyao Zhang [1], Yuxi Zheng [1], Chenhao Guan [1], Weiqiong Huang [2] and Nan Fang [2]

[1] State Grid Fujian Economic Research Institute, Fuzhou 350013, China
[2] State Grid Zhangzhou Electric Power Supply Company, Zhangzhou 363000, China
* Correspondence: jwxue210@163.com

Abstract

Demand-side flexibility from buildings and other urban electricity consumers is increasingly important for renewable-energy integration and net-zero urban energy systems. However, when many consumers respond to the same locational electricity–carbon signals, their collective actions can alter market-clearing states and invalidate the signals used by later participants. An adaptive re-clearing strategy is developed for coordinating such responses under a limited security-constrained economic dispatch (SCED) budget. Multi-period market clearing is formulated as a convex optimization problem parameterized by nodal demand, and sequential participation is represented as a discretized continuously refreshed path. For each candidate batch, one full response step is compared with two re-cleared half steps. Their endpoint difference is used to accept or reject the batch and adjust its subsequent size. Fine-grid paths and constrained Richardson extrapolation are used for validation. In the IEEE 14-bus system, the static locational marginal carbon emission (LMCE) predicted a 34.45 tCO_2 reduction under large-scale participation, whereas only 4.22 tCO_2 was realized after re-clearing. Across five participation scales, the strategy adapted its update frequency without a predefined batch number and remained within 0.605 MWh of the best budget-feasible fixed scheme. The method provides a coordination mechanism for carbon-responsive urban demand that adaptively selects signal-update locations within a prescribed SCED budget, without requiring a predefined number of response groups.

Keywords: urban energy systems; demand-side flexibility; locational marginal emissions; adaptive re-clearing

Check for updates

Academic Editor: Tapas Mallick

Received: 28 September 2026
Revised: 30 October 2026
Accepted: 2 November 2026
Published: 7 November 2026

Copyright: © 2026 by the authors. Licensee MDPI, Basel, Switzerland. This article is an open access article distributed under the terms and conditions of the Creative Commons Attribution (CC BY) license.

1. Introduction

As power systems transition towards high shares of renewable energy and lower carbon emissions, demand-side flexibility is evolving from a conventional peak-shaving resource into an active participant in electricity markets and carbon mitigation [1,2]. Locational marginal prices reflect the marginal cost of supplying electricity across locations and time, whereas locational marginal emissions quantify the change in system-wide emissions caused by an incremental change in demand [3]. Their joint use could therefore guide the spatial and temporal redistribution of flexible demand while balancing economic and environmental objectives [4]. However, low-price periods do not necessarily coincide with low-emission periods. Transmission congestion, generation portfolios, reserve requirements, storage states, and renewable generation variability can all cause electricity prices and marginal emission signals to diverge. More importantly, when a large population of flexible

consumers responds to the same marginal signals, their collective actions alter the demand profile, market-clearing outcome, and active operating constraints, thereby progressively invalidating the signals on which those actions were based [5]. Although frequent market re-clearing can refresh these signals, it imposes a substantial computational burden on SCED. Determining when signals should be updated and how participating consumers should be grouped under a limited re-clearing budget is therefore essential for enabling marginal electricity–carbon signals to support demand response at scale.

Research on electricity-related carbon signals has progressively shifted from attribution-based accounting towards intervention-oriented marginal metrics. Carbon-emission-flow methods trace embodied emissions through network power flows and allocate them to individual nodes or market participants. Recent extensions have incorporated prosumers, distributed energy resources, and storage [6], while high-spatiotemporal-resolution models have enabled hourly, nodal-level carbon accounting [7]. These approaches characterize the carbon responsibility associated with electricity consumption but do not directly quantify how total system emissions respond to an incremental change in demand. Locational marginal emissions (LMEs) address this distinction by differentiating system-wide emissions with respect to nodal and temporal demand. Implicit-differentiation methods have enabled the calculation of dynamic LMEs under intertemporal constraints such as generator ramping and energy storage [8] and have subsequently been extended to active and reactive demand in distribution networks [9]. Parallel and decentralized differentiation schemes have further improved the computational scalability of emission-sensitivity calculations for large power systems [10]. Nevertheless, computational accuracy does not guarantee that a marginal signal remains valid for a finite demand adjustment. Empirical evaluation also indicates that modeled marginal emission factors can exhibit materially different behavioral consistency [11]. More critically, the validity ranges of locational marginal emission factors can be small or even vanish under network congestion [3]. Therefore, existing studies have substantially advanced the resolution and computation of electricity-related carbon signals but have not fully addressed how their accuracy should be maintained when aggregate demand response moves the system beyond the local operating region in which those signals were derived.

Demand-side decarbonization has been investigated mainly through price- and incentive-based demand response and carbon-aware system operation. By comparing real-time pricing with direct load control, Miri and McPherson showed that both mechanisms can enhance network flexibility, reduce wind curtailment, and improve operating costs, although their benefits depend on the availability of sufficient flexible demand [12]. Learning-based approaches have subsequently been introduced to improve pricing decisions under complex consumer behavior. Salazar et al. combined price- and incentive-based schemes with reinforcement learning to improve load shifting and load factors [13], whereas Qian et al. developed an offline deep reinforcement learning framework that learns pricing strategies from suboptimal historical data while accounting for uncertainties in demand and electricity prices [14]. These studies primarily optimize economic performance, peak demand, or renewable-energy accommodation rather than the emissions realized after demand redistribution. Carbon-oriented studies, in contrast, have examined long-term renewable deployment and carbon-pricing policies [15], household carbon compensation through voluntary offsets [16], and low-carbon dispatch incorporating seasonal carbon-flow balance and stepped carbon trading [17]. Although these two research streams demonstrate the potential of demand flexibility and carbon regulation, they generally treat price signals, emission factors, or dispatch conditions as exogenously specified or centrally optimized. Consequently, limited attention has been paid to whether load shifting induced by an electricity–carbon signal still delivers the anticipated emission reduction after market

re-clearing, particularly when collective demand response changes marginal generators, network congestion, and intertemporal operating constraints.

Beyond their calculation, locational marginal emission signals have been increasingly used to guide carbon-aware demand-side decisions. Park et al. developed an LME-based load-shifting strategy for active distribution networks and demonstrated the emission-reduction potential of spatially differentiated demand flexibility [18]. Hu et al. further incorporated transmission-network impacts into large-scale electric-vehicle deployment planning, using paired locational marginal prices and marginal emission factors to characterize the spatial heterogeneity of long-term charging emissions [19]. However, these applications optimize demand-side decisions against marginal signals computed from a given system state. Because such signals represent local sensitivities, their validity may deteriorate when a finite load adjustment changes congestion patterns or marginal generators; indeed, their valid ranges can be small or even vanish under stressed network conditions [3]. A related body of research has improved the coordination and computational efficiency of coupled market operations. Equilibrium analysis and learning have been employed to characterize coordinated transaction scheduling across interconnected electricity markets [20], while multiparametric programming and decomposition have enabled efficient decentralized tracking of coordinated economic-dispatch solutions [21]. These studies provide important mechanisms for market coordination and repeated optimization but generally rely on predefined iterative procedures and do not determine when a marginal electricity–carbon signal should be recomputed as aggregate demand response accumulates. Consequently, an unresolved problem is how to allocate a limited SCED re-clearing budget online, adaptively selecting response batches so that the resulting discrete participation path remains close to the continuously refreshed benchmark without requiring prior knowledge of an appropriate fixed batch number.

To address these issues, this study proposes an adaptive batch-updating method for locational marginal electricity–carbon signals under a limited SCED re-clearing budget. The multi-period market-clearing problem is first formulated as a convex optimization problem parameterized by nodal demand. Its Karush–Kuhn–Tucker (KKT) system characterizes the local mappings from demand to electricity prices and marginal emissions within a fixed active set, while aggregator behavior is represented by a strongly convex response problem subject to energy-neutrality and flexibility constraints. Sequential consumer participation is then described as a continuous path. The endpoint difference between one full response step and two re-cleared half steps provides an observable local error estimate for accepting or rejecting a candidate batch and adjusting the subsequent batch size. Finally, fine-grid paths and constrained extrapolation are used as numerical references to compare the adaptive method with budget-feasible fixed grouping across different participation scales. Price–carbon misalignment, path-integral residuals, active-set changes, and closed-loop gains are further employed to explain the mechanism underlying static-signal invalidation. The main contributions of this paper can be summarized as follows:

(1) A budget-constrained online batch-selection problem is formulated for updating locational marginal electricity–carbon signals. Different from conventional methods in which marginal signals are treated as fixed inputs or the number of response groups is predetermined, the endogenous feedback among aggregate demand response, market-clearing states, and subsequent signals is explicitly considered. A unified evaluation framework is thereby established to relate the SCED budget, signal-update frequency, response-path accuracy, operating cost, and realized emissions.

(2) An error-estimate-driven adaptive batch-updating method is developed by representing sequential consumer participation as a discrete approximation of a continuously refreshed response path. For each candidate macro step, the endpoint obtained from one

full response step is compared with that obtained from two half steps separated by SCED re-clearing. The resulting coarse–fine difference is used to accept or reject the candidate batch and adjust the subsequent batch size, without requiring a predefined group number or active-set validity radius.

(3) A multi-perspective framework is established to diagnose the endogenous invalidation of static electricity–carbon signals. Price–carbon misalignment, marginal-emission path-integral residuals, market active-set changes, and intertemporal feedback gains are jointly examined to distinguish initial signal inconsistency from response-induced signal distortion. Through budget-matched comparisons across multiple participation scales, the proposed method is shown to adapt its update frequency and track the accuracy frontier of fixed-grouping schemes without requiring the appropriate batch number to be known in advance.

2. Parametric Market Clearing and Demand-Response Mappings

This section establishes the mappings that connect market clearing, nodal electricity–carbon signals, and aggregator response. The multi-period SCED problem is first formulated as a convex quadratic program parameterized by nodal demand. The KKT is then used to characterize the local market mapping within a fixed active set. The public energy locational marginal price (LMP), the complete derivative of the market value function, and the LMCE are subsequently distinguished before constructing the electricity–carbon signal delivered to demand aggregators. Finally, load shifting is represented as a strongly convex projection problem, which yields a piecewise-affine and non-expansive response mapping. These mappings provide the basis for analyzing endogenous signal invalidation and budget-constrained re-clearing in the subsequent section.

2.1. Market Clearing Parameterized by Nodal Demand

Consider a multi-period power system with the bus set $\mathcal{N}$, time set $\mathcal{T}$, conventional generator set $\mathcal{G}$, renewable generator set $\mathcal{R}$, and transmission-line set $\mathcal{L}$. Nodal demands over all buses and periods are stacked in a parameter vector $D \in \mathbb{R}^{n_D}$. The decision vector $z \in \mathbb{R}^{n_z}$ collects conventional generation, renewable utilization, spinning reserve, line flows, voltage angles, storage charging and discharging powers, and state of charge. Under quadratic generation costs and a direct-current (DC) network representation, the multi-period SCED problem is written compactly as

$$Q^{\mathrm{M}}(D) = \min_{z}\left\{\frac{1}{2}z^{\mathsf{T}}Hz + c^{\mathsf{T}}z\right\}, \tag{1}$$

$$\text{s.t.} \qquad Az = b + BD, \qquad Gz \le h + SD, \tag{2}$$

where $H \succeq 0$ and c are the quadratic and linear cost coefficients, respectively. The equality constraints include nodal power balance, direct-current power flow, the reference angle, and intertemporal storage dynamics. The inequalities represent generation limits, ramping limits, reserve requirements, transmission limits, load shedding, and storage power limits. Matrices B and S specify how nodal demand enters the equality and inequality right-hand sides. Demand may therefore affect not only nodal balance but also operating requirements such as spinning reserve.

Let ν and $\eta \ge 0$ denote the multipliers associated with the equality and inequality constraints, respectively, and let $\mathcal{A}(D)$ be the active inequality set at D. The Lagrangian is

$$\mathcal{L}(z, \nu, \eta; D) = \frac{1}{2}z^{\mathsf{T}}Hz + c^{\mathsf{T}}z + \nu^{\mathsf{T}}(Az - b - BD) + \eta^{\mathsf{T}}(Gz - h - SD). \tag{3}$$

For a fixed active set $\mathcal{A}$, the KKT conditions become

$$Hz^* + c + A^\top \nu^* + G_{\mathcal{A}}^\top \eta_{\mathcal{A}}^* = 0, \tag{4a}$$

$$Az^* = b + BD, \tag{4b}$$

$$G_{\mathcal{A}} z^* = h_{\mathcal{A}} + S_{\mathcal{A}} D, \qquad \eta_{\mathcal{A}}^* \geq 0. \tag{4c}$$

Define $J_z = \partial z^*/\partial D$, $J_\nu = \partial \nu^*/\partial D$, and $J_\eta = \partial \eta_{\mathcal{A}}^*/\partial D$. Implicit differentiation of Equation (4) gives

$$\begin{bmatrix} H & A^\top & G_{\mathcal{A}}^\top \\ A & 0 & 0 \\ G_{\mathcal{A}} & 0 & 0 \end{bmatrix} \begin{bmatrix} J_z \\ J_\nu \\ J_\eta \end{bmatrix} = \begin{bmatrix} 0 \\ B \\ S_{\mathcal{A}} \end{bmatrix}. \tag{5}$$

The local analysis assumes the linear independence constraint qualification, strict complementarity, and nonsingularity of the reduced KKT matrix on the relevant variable subspace. A unique and continuous market solution is selected if degeneracy is present. For a non-degenerate linear dispatch model, the same argument applies while the optimal basis remains unchanged.

Proposition 1 (Piecewise structure of the market mapping)**.** *Under the stated regularity conditions, $z^*(D)$, $\nu^*(D)$, and $\eta_{\mathcal{A}}^*(D)$ are affine in D within a fixed active set $\mathcal{A}$. If total generation emissions are linear in conventional generator outputs, $E(D)$ is affine in the same region, the energy LMP is piecewise affine in D, and the exact LMCE is constant in every non-degenerate critical region.*

Proof. For a fixed $\mathcal{A}$, the coefficient matrix in Equation (5) is independent of D. Hence, J_z, J_ν, and J_η are constant, and integration yields affine primal and dual solutions. A new affine segment is entered when the primal slack of an inactive constraint or the multiplier of an active constraint reaches zero. The local sensitivity therefore cannot be extrapolated to an arbitrary demand displacement without verifying that the active set remains unchanged. □

2.2. Dynamic LMP, LMCE, and the Electricity–Carbon Signal

Ramping constraints, reserve requirements, and storage dynamics couple operating decisions across time. A nodal–temporal price or emission sensitivity must therefore be interpreted as the marginal response of the complete horizon-wide problem. The public energy LMP should first be distinguished from the full derivative of the market value function. Under the sign convention in Equation (3), the public energy LMP is

$$\lambda^{\mathrm{E}}(D) = -B^\top \nu^*(D). \tag{6}$$

If demand also enters the right-hand side of inequality constraints, the envelope theorem gives

$$\pi(D) = \nabla_D Q^{\mathrm{M}}(D) = -B^\top \nu^*(D) - S^\top \eta^*(D). \tag{7}$$

Thus, $\pi = \lambda^{\mathrm{E}}$ only when demand does not parameterise any inequality constraint. In the present model, the spinning-reserve requirement in period t contains $0.05 \sum_i D_{i,t}$. Using a positive scarcity-price convention for the reserve constraint gives

$$\pi_{i,t} = \lambda_{i,t}^{\mathrm{E}} + 0.05\, \xi_t, \tag{8}$$

where ξ_t is the reserve scarcity price. The published energy price is therefore not, in general, the complete demand derivative of the SCED objective.

Let R_P select conventional generator outputs from z, and let e collect their emission factors. Total system emissions are

$$E(D) = e^\top R_P z^*(D). \tag{9}$$

The exact LMCE is defined as the gradient of total emissions with respect to nodal–temporal demand:

$$m(D) = \nabla_D E(D) = J_z(D)^\top R_P^\top e. \tag{10}$$

Proposition 1 implies that $m(D)$ is constant while a non-degenerate market active set is retained and may jump when the active set changes. To avoid selecting an arbitrary one-sided derivative at a degenerate point and to remain consistent with operational re-clearing, the signal released to aggregators uses a forward finite-difference LMCE:

$$m_{i,t}^{\delta_m}(D) = \frac{E\big(D + \delta_m e_{i,t}\big) - E(D)}{\delta_m}, \qquad \delta_m = 0.1\ \text{MWh}, \tag{11}$$

where $e_{i,t}$ is the unit vector associated with bus i and period t. The complete multi-period SCED problem is re-solved at every perturbation point. If $E(D)$ is continuous and piecewise affine, m^{δ_m} is an interval-averaged slope over a displacement of length δ_m. A slope discontinuity is consequently spread over a transition band with a width of approximately δ_m. This construction provides a single-valued numerical signal, but it remains dependent on the perturbation size and should not be conflated with an exact one-sided derivative.

The market objective already internalizes a carbon-cost component. Let C^{op} denote physical operating cost and $\bar{\mu}$ the carbon price embedded in market clearing. Then

$$Q^{\text{M}}(D) = C^{\text{op}}(D) + \bar{\mu} E(D). \tag{12}$$

An aggregator receives an electricity–carbon signal that combines the public energy LMP with an additional demand-side carbon value μ_a:

$$s^{\delta_m}(D) = \lambda^{\text{E}}(D) + \mu_a m^{\delta_m}(D). \tag{13}$$

If policy specifies a total carbon value μ_{total}, the additional component should be set to $\mu_a = \mu_{\text{total}} - \bar{\mu}$ to prevent double counting. Moreover, s^{δ_m} is generally different from the complete social-value gradient. It uses the energy LMP rather than π, and the finite-difference LMCE rather than the exact m. Accordingly, λ^{E} is used to drive the aggregator response, π is retained for checking the path integral of the market objective, and the change in physical operating cost is recovered as

$$\Delta C^{\text{op}} = \Delta Q^{\text{M}} - \bar{\mu}\, \Delta E. \tag{14}$$

2.3. Aggregator Projection Response and Non-Expansiveness

Let x_i denote the load adjustment of aggregator i over $|\mathcal{T}|$ periods, where positive and negative entries represent load increases and reductions, respectively. Given the signal s_i, the aggregator balances signal expenditure against a quadratic discomfort cost:

$$X_i(s_i) = \arg\min_{x_i \in \mathcal{X}_i} \left\{ s_i^\top x_i + \frac{1}{2} x_i^\top K_i x_i \right\}, \tag{15}$$

$$\mathcal{X}_i = \left\{ x_i \,\middle|\, \mathbf{1}^\top x_i = 0, \quad -r_{i,t}^- \le x_{i,t} \le r_{i,t}^+,\ \forall t \in \mathcal{T} \right\}. \tag{16}$$

Here, $K_i \succeq \kappa_i I$ with $\kappa_i > 0$, while $r_{i,t}^-$ and $r_{i,t}^+$ specify downward and upward flexibility. The energy-neutrality constraint excludes net energy creation or curtailment and permits only intertemporal shifting. Strong convexity of the objective and closed convexity of $\mathcal{X}_i$ guarantee a unique response. Equivalently, Equation (15) is a weighted projection:

$$X_i(s_i) = \Pi_{\mathcal{X}_i}^{K_i}\big(-K_i^{-1} s_i\big), \qquad \Pi_{\mathcal{X}_i}^{K_i}(y) = \arg\min_{x \in \mathcal{X}_i} \frac{1}{2} \|x - y\|_{K_i}^2. \tag{17}$$

Let $\mathcal{H}$ denote the set of active upper and lower response bounds. For a fixed $\mathcal{H}$, combine energy neutrality and the active bounds as $A_{\mathcal{H}} x_i = b_{\mathcal{H}}$. The corresponding KKT system is

$$\begin{bmatrix} K_i & A_{\mathcal{H}}^{\mathsf{T}} \\ A_{\mathcal{H}} & 0 \end{bmatrix} \begin{bmatrix} x_i \\ y_{\mathcal{H}} \end{bmatrix} = \begin{bmatrix} -s_i \\ b_{\mathcal{H}} \end{bmatrix}. \tag{18}$$

The response is therefore affine in s_i within a fixed user active set.

Proposition 2 (Piecewise affinity and non-expansiveness of the response)**.** *If $K_i \succeq \kappa_i I$ with $\kappa_i > 0$, there exist a vector $q_{i,\mathcal{H}}$ and a positive-semidefinite matrix $M_{i,\mathcal{H}}$ such that, within any fixed user active set $\mathcal{H}$,*

$$X_i(s_i) = q_{i,\mathcal{H}} - M_{i,\mathcal{H}} s_i, \qquad M_{i,\mathcal{H}} \succeq 0. \tag{19}$$

For any two signals $s_i^{(1)}$ and $s_i^{(2)}$, the response satisfies

$$\left\| X_i\left(s_i^{(1)}\right) - X_i\left(s_i^{(2)}\right) \right\|_2 \leq \frac{1}{\kappa_i} \left\| s_i^{(1)} - s_i^{(2)} \right\|_2. \tag{20}$$

Proof. The coefficient matrix in Equation (18) is independent of s_i for a fixed $\mathcal{H}$, which directly yields Equation (19). For two optimal responses, strong convexity and monotonicity of the normal cone of $\mathcal{X}_i$ imply

$$\kappa_i \|\Delta x_i\|_2^2 \leq -\langle \Delta s_i, \Delta x_i \rangle \leq \|\Delta s_i\|_2 \|\Delta x_i\|_2, \tag{21}$$

where $\Delta x_i = X_i(s_i^{(1)}) - X_i(s_i^{(2)})$ and $\Delta s_i = s_i^{(1)} - s_i^{(2)}$. Dividing by $\|\Delta x_i\|_2$ when $\Delta x_i \neq 0$ proves Equation (20); the result is immediate when $\Delta x_i = 0$. □

Proposition 2 shows that a finite signal perturbation cannot be amplified without bound by an individual aggregator. The worst-case sensitivity is controlled by the strong-convexity modulus κ_i: a smaller κ_i produces a more responsive load-shifting decision. Nevertheless, the aggregate market impact increases with the number and capacity of participating aggregators. Mapping all responses back to the nodal–temporal demand coordinates gives

$$D^+ = D + \sum_i P_i X_i\left(s_i^{\delta_m}(D)\right), \tag{22}$$

where P_i embeds aggregator i into the system demand vector. Equation (22) closes the market-clearing–signal–response feedback loop and provides the common starting point for analyzing local signal validity, endogenous invalidation, and batch re-clearing.

3. Diagnosis of Static-Signal Invalidation

Section 2 showed that, within a fixed market active set, the dispatch solution is affine in nodal demand and the exact LMCE is constant in a non-degenerate critical region. A static electricity–carbon signal is therefore not intrinsically inaccurate. Its validity is local and can be lost when the aggregate response crosses a generation, transmission, reserve, or storage constraint boundary.

This section diagnoses static-signal invalidation from three complementary perspectives. First, a path-integral residual quantifies the discrepancy between the static LMCE prediction and the realized re-cleared outcome, while directional validity radii explain its local structural origin. Second, price–carbon misalignment and critical carbon values identify the risk of a cost-reducing but emission-increasing response. Third, a closed-loop gain characterizes the local feedback strength between market signals and aggregate demand response. These quantities provide interpretation and warnings. Only the directly observable coarse–fine difference e_ω is used by the adaptive batching method developed in the next section.

3.1. Path-Integral Residual and the Signal-Invalidation Mechanism

Let D^0 denote the baseline demand and let ΔD be the aggregate demand adjustment derived from the static signal. The response path connecting the baseline and the final demand is defined as

$$D(\tau) = D^0 + \tau \Delta D, \qquad \tau \in [0,1]. \tag{23}$$

The market value function $Q^{\mathrm{M}}(D)$ and the system emission function $E(D)$ are differentiable almost everywhere along this path. Their realized changes can therefore be expressed as

$$\Delta Q^{\mathrm{M}} = \int_0^1 \pi\big(D^0 + \tau \Delta D\big)^{\mathsf{T}} \Delta D \, \mathrm{d}\tau, \tag{24}$$

and

$$\Delta E = \int_0^1 m\big(D^0 + \tau \Delta D\big)^{\mathsf{T}} \Delta D \, \mathrm{d}\tau, \tag{25}$$

where

$$\pi(D) = \nabla_D Q^{\mathrm{M}}(D), \qquad m(D) = \nabla_D E(D) \tag{26}$$

are the complete demand derivative of the market value function and the exact LMCE, respectively. If the supply-side market objective contains an embedded carbon value $\bar{\mu}$, the corresponding physical operating-cost change is recovered as

$$\Delta C^{\mathrm{op}} = \Delta Q^{\mathrm{M}} - \bar{\mu} \Delta E. \tag{27}$$

A static-LMCE scheme retains the baseline marginal emission signal $m(D^0)$ throughout the entire response process. Its first-order prediction of the emission change is

$$\widehat{\Delta E}_{\mathrm{stat}} = m(D^0)^{\mathsf{T}} \Delta D. \tag{28}$$

The discrepancy between the realized emission change and this static prediction is

$$\begin{aligned} R_{\mathrm{stat}} &= \Delta E - \widehat{\Delta E}_{\mathrm{stat}} \\ &= \int_0^1 \big[m\big(D^0 + \tau \Delta D\big) - m(D^0) \big]^{\mathsf{T}} \Delta D \, \mathrm{d}\tau. \end{aligned} \tag{29}$$

Equation (29) gives a direct interpretation of static-signal invalidation. The residual is not an unspecified higher-order term. It is the accumulated effect of the difference between the baseline LMCE and the marginal emission signals encountered along the realized response path. Consequently, a static signal becomes unreliable when the collective response materially changes the market state and hence the marginal signal faced by subsequent participants.

Proposition 3 (Exactness of the static LMCE within a critical region)**.** *Suppose that generator emissions are linear in conventional generator outputs and that $D(\tau)$ remains within one non-degenerate market critical region. Then*

$$m\big(D(\tau)\big) = m(D^0), \qquad \forall \tau \in [0,1], \tag{30}$$

and, consequently,

$$R_{\mathrm{stat}} = 0. \tag{31}$$

Proof. Proposition 1 establishes that the optimal market solution $z^*(D)$ is affine in D within a fixed active set. Under the linear generator-emission model, $E(D)$ is therefore affine and its gradient $m(D)$ is constant in the same critical region. Substituting Equation (30) into Equation (29) gives $R_{\mathrm{stat}} = 0$. □

The static LMCE is thus exact, rather than merely approximately correct, as long as the complete response path remains within its initial critical region. Its main structural error arises after the path crosses one or more active-set boundaries. If the exact LMCE has bounded total variation along $D(\tau)$, the residual satisfies

$$|R_{\text{stat}}| \leq \text{TV}_m[D(\tau)]\|\Delta D\|_2, \tag{32}$$

where $\text{TV}_m[D(\tau)]$ denotes the total variation of the LMCE along the response path. Equation (32) shows that static-signal error is jointly determined by the response magnitude and the structural variation of the marginal emission signal.

To compare responses of different magnitudes, the relative static-signal distortion is defined as

$$\eta_{\text{stat}} = \frac{|R_{\text{stat}}|}{|\Delta E| + \varepsilon}, \tag{33}$$

where $\varepsilon > 0$ prevents numerical singularity when the realized emission change is close to zero. A value $\eta_{\text{stat}} > 1$ means that the static prediction error exceeds the magnitude of the realized emission change; it does not represent an emission change greater than 100%.

A complementary endpoint indicator is

$$\chi_{\mathcal{A}} = \mathbf{1}\{\mathcal{A}(D^0 + \Delta D) \neq \mathcal{A}(D^0)\}. \tag{34}$$

The condition $\chi_{\mathcal{A}} = 1$ confirms that the baseline and endpoint belong to different active-set regions. It does not count intermediate switching events and, by itself, does not determine whether the operating cost or emissions improve.

For a unit response direction q, with $\|q\|_2 = 1$, the local range over which the baseline active set remains valid can be represented compactly by

$$\alpha_{\mathcal{A}}(q) = \sup\{\alpha \geq 0 : \mathcal{A}(D^0 + \xi q) = \mathcal{A}(D^0),\ \forall \xi \in [0, \alpha]\}. \tag{35}$$

Within a non-degenerate critical region, this radius can equivalently be obtained from the first inactive-constraint slack or active-constraint multiplier that reaches zero under the affine KKT sensitivity. The detailed slack-by-slack and multiplier-by-multiplier derivation is omitted here because $\alpha_{\mathcal{A}}(q)$ is not used by the proposed batch-size controller.

If $\Delta D = \alpha q$ and $\alpha < \alpha_{\mathcal{A}}(q)$, the fixed-active-set sensitivity remains valid along the complete response direction and Proposition 3 applies. When $\alpha \geq \alpha_{\mathcal{A}}(q)$, the local guarantee is lost, but this condition alone does not establish the magnitude or direction of the resulting economic and carbon effects.

In the numerical study, the analytical radius is not evaluated from the complete primal-dual sensitivity system. Instead, a re-clearing-based safe-side estimate, denoted by $\alpha^-(q)$, is constructed as an auxiliary diagnostic. Its scanning, bisection, tolerance, and interpretation are presented together with the numerical implementation in Chapter 3.

For subsequent numerical comparison, define the safe-side radius ratio as

$$r_\alpha = \frac{\|\Delta D\|_2}{\alpha^-(q)}. \tag{36}$$

A value $r_\alpha < 1$ means that the planned response remains within the numerically tested safe side, whereas $r_\alpha \geq 1$ means that it reaches or exceeds the first detected active-state boundary. Because $\alpha^-(q)$ depends on a finite scan and an active-state tolerance, $r_\alpha < 1$ is not an analytical validity certificate.

For a finite-difference LMCE m^{δ_m}, the residual may additionally contain a smoothing error when the perturbation stencil crosses an active-set boundary. Therefore, R_{stat}, η_{stat}, and $\chi_{\mathcal{A}}$ are retained as diagnostic quantities for explaining when and why a static signal becomes unreliable. None of these quantities directly determines the adaptive batch size; the proposed method uses the observable one-step–two-half-step difference introduced in the following chapter.

3.2. Price–Carbon Misalignment and Critical Carbon Values

The path-integral residual explains why a signal becomes stale as aggregate participation increases. The initial response direction, however, is governed by the temporal ordering of electricity prices and marginal emissions. If a low-price period has a high LMCE, price-based load shifting may reduce expenditure while increasing system emissions.

Consider first an unconstrained response with identical discomfort coefficients across periods. Let

$$P = I - \frac{1}{T}\mathbf{1}\mathbf{1}^{\mathsf{T}} \tag{37}$$

be the demeaning projection and let $K_i = \kappa_i I$. Under a carbon value μ, aggregator i responds to $\lambda_i + \mu m_i$ as

$$x_i^*(\mu) = -\frac{1}{\kappa_i} P(\lambda_i + \mu m_i). \tag{38}$$

For $\mu = 0$, the aggregator responds only to electricity prices. The first-order emission change is

$$\begin{aligned} \Delta E_i^{(1)}(0) &= m_i^{\mathsf{T}} x_i^*(0) \\ &= -\frac{1}{\kappa_i} m_i^{\mathsf{T}} P \lambda_i \\ &= -\frac{T}{\kappa_i} \operatorname{Cov}(m_i, \lambda_i). \end{aligned} \tag{39}$$

Consequently,

$$\operatorname{Cov}(m_i, \lambda_i) < 0 \tag{40}$$

is a local condition for a cost-reducing but emission-increasing price response. Equation (39) applies only when $K_i = \kappa_i I$ and no response bound is active. For a general K_i, the energy-neutral projection must be evaluated in the K_i^{-1} metric, and the ordinary covariance expression is no longer sufficient.

The ranking conflict between electricity prices and LMCEs at bus i is summarized by

$$\mathrm{MI}_i = \frac{N\{(\lambda_{i,t} - \lambda_{i,\tau})(m_{i,t} - m_{i,\tau}) < 0\}}{N\{t \neq \tau\}}. \tag{41}$$

For a 24-period horizon, the denominator contains 24×23 ordered period pairs. A pair is counted as conflicting when the price difference and LMCE difference have opposite signs. Dimensional tolerances of 10^{-7} yuan/MWh and 10^{-7} tCO_2/MWh are applied to price and LMCE differences, respectively. Tied values are excluded from the numerator but retained in the fixed denominator.

A larger MI_i indicates more frequent ranking conflicts, but it does not quantify the resulting emission increase and should not be interpreted as a robust bus ranking. The index remains sensitive to the operating point, numerical tolerances, and the finite-difference LMCE step.

Actual aggregator responses are subject to energy neutrality and power bounds. Their KKT conditions are

$$s(\mu) + Kx + \mathbf{1}\nu + \alpha^+ - \alpha^- = 0, \tag{42a}$$

$$\mathbf{1}^{\mathsf{T}} x = 0, \qquad -r^- \le x \le r^+, \tag{42b}$$

$$\alpha^+ \odot (x - r^+) = 0, \qquad \alpha^- \odot (-x - r^-) = 0, \qquad \alpha^+, \alpha^- \ge 0. \tag{42c}$$

For a fixed user active set $\mathcal{H}$, the response is affine in μ:

$$x_{\mathcal{H}}(\mu) = a_{\mathcal{H}} + b_{\mathcal{H}}\mu. \tag{43}$$

If the baseline market LMCE is retained, the first-order emission change is also affine:

$$\Delta E^{(1)}_{\mathcal{H}\ell}(\mu) = m^{\mathsf{T}} x_{\mathcal{H}\ell}(\mu) = c_{\mathcal{H}\ell} + d_{\mathcal{H}\ell}\mu. \tag{44}$$

For $d_{\mathcal{H}\ell} \neq 0$, the candidate critical carbon value in this user active region is

$$\mu^{*}_{\mathcal{H}\ell} = -\frac{c_{\mathcal{H}\ell}}{d_{\mathcal{H}\ell}}. \tag{45}$$

This value is valid only if it lies within the interval that retains $\mathcal{H}\ell$. Otherwise, the adjacent user active set must be considered.

Three levels of critical carbon value are distinguished.

1. The unconstrained covariance threshold neglects response bounds and assumes identical temporal discomfort coefficients. It captures only the initial direction implied by price–carbon covariance. This threshold is 0 yuan/tCO_2 in the present case.
2. The bounded KKT threshold retains energy neutrality, response bounds, and heterogeneous discomfort costs while fixing the baseline market signals. Equations (43)–(45) give an effective threshold of 116.83 yuan/tCO_2.
3. The re-cleared threshold recomputes both the aggregator response and market clearing for every candidate carbon value and locates the sign change in the realized endpoint emissions. This threshold is 131.63 yuan/tCO_2 in the present case.

These values correspond to different model layers rather than numerical approximations of one universal threshold. The covariance threshold diagnoses price–carbon misalignment, the bounded KKT threshold accounts for user-side constraints, and the re-cleared threshold includes market feedback. The critical carbon values are explanatory diagnostics and are not used by the adaptive batching algorithm.

3.3. Closed-Loop Gain as an Auxiliary Diagnostic

The path-integral residual measures the accumulated error of a static signal over a finite response path. The closed-loop gain instead characterizes the local amplification of an infinitesimal market-state perturbation through the signal–response chain.

Let $M^{\mathrm{rem}}_{\mathcal{H}\ell} = -\partial X_{\mathrm{rem}}/\partial s$ denote the local response sensitivity of the remaining population, and let $J_s = \partial s/\partial D$ denote the local Jacobian of the electricity–carbon signal. If ϱ is the scale of the population that has not yet responded, the closed-loop spectral gain is defined as

$$\Gamma_2 = \left\| \varrho M^{\mathrm{rem}}_{\mathcal{H}\ell} J_s \right\|_2. \tag{46}$$

The quantity Γ_2 measures the maximum first-order amplification of an infinitesimal market-state perturbation by the remaining responsive population. A value $\Gamma_2 < 1$ indicates local non-expansiveness of the signal–response chain, whereas $\Gamma_2 \geq 1$ means only that this local guarantee is lost.

The gain is an offline auxiliary diagnostic and is not used to accept, reject, or resize a candidate batch. Moreover, $\Gamma_2 < 1$ does not guarantee that a static signal remains accurate over a finite response path. A large response may cross several market active-set boundaries even when the local gain remains below unity. The resulting path-integral residual R_{stat}, rather than local first-order amplification, is the main source of static-signal invalidation in the present case study.

3.4. Summary of Diagnostic Quantities

The quantities introduced in this section are divided into a direct observable used by the main method and auxiliary diagnostic measures. The subsequent adaptive algorithm uses only the coarse–fine endpoint difference e_ω to accept, reject, and resize a candidate batch. Table 1 summarizes these quantities and their roles in the proposed framework.

Table 1. Diagnostic quantities and their roles in the proposed framework.

Quantity	Definition	Interpretation	Role
e_ω	$\|\Psi_\omega(D) - \Phi_\omega(D)\|_2$	Endpoint difference between one full response step and two re-cleared half steps	Direct observable used by the main adaptive method
R_{stat}	$\Delta E - m(D^0)^\top \Delta D$	Path-integral residual of the static LMCE prediction	Auxiliary invalidation diagnostic
η_{stat}	$\|R_{\text{stat}}\|/(\|\Delta E\| + \varepsilon)$	Static prediction error relative to the realized emission change	Auxiliary scale-comparison metric
$\chi_{\mathcal{A}}$	$\mathbf{1}\{\mathcal{A}(D^1) \neq \mathcal{A}(D^0)\}$	Difference between baseline and endpoint market active sets	Auxiliary structural indicator
$\alpha_{\mathcal{A}}(q)$	First primal or dual margin reaching zero	Analytical validity radius along direction q	Theoretical diagnostic only
$[\alpha^-, \alpha^+]$	Re-clearing scan and bisection bracket	Numerical bracket of the first observed active-state change	Auxiliary warning metric
MI_i	Fraction of oppositely ranked price–LMCE period pairs	Temporal price–carbon ranking conflict	Auxiliary direction diagnostic
$\mu^*_{\mathcal{H}\ell}$	$-c_{\mathcal{H}\ell}/d_{\mathcal{H}\ell}$	Critical carbon value within a fixed user active set	Auxiliary interpretation metric
Γ_2	$\|\varrho M^{\text{rem}}_{\mathcal{H}\ell} J_s\|_2$	Worst-case local amplification over all perturbation directions	Offline auxiliary diagnostic

For completeness, define the coarse endpoint obtained by applying a response fraction ω under the current signal as

$$\Phi_\omega(D) = D + \omega f(D). \tag{47}$$

Applying the same total fraction through two half steps and re-clearing at the midpoint gives

$$\Psi_\omega(D) = \Phi_{\omega/2}\big(\Phi_{\omega/2}(D)\big). \tag{48}$$

The resulting coarse–fine difference is

$$e_\omega(D) = \|\Psi_\omega(D) - \Phi_\omega(D)\|_2. \tag{49}$$

Unlike the analytical radius, critical carbon value, or full market Jacobian, e_ω is obtained directly from candidate re-clearing outcomes. It therefore exposes the local nonlinearity and signal-update effect without requiring an explicit active-set sensitivity model.

4. Error-Estimate-Driven Batch Updating

The diagnostics developed in Section 3 explain why a static signal becomes unreliable, but they do not determine where market re-clearing should occur or how much responsive demand should be admitted in each batch. In day-ahead operation, computational capacity and market timing impose a finite re-clearing budget. Re-solving the complete SCED problem after every individual response is therefore impractical.

This section formulates online batch selection under a limited SCED budget. An ordered participation path is first introduced to distinguish sequential one-time responses from autonomous fixed-point iterations. A directly observable discrepancy between one full response step and two re-cleared half steps is then used to accept, reject, and resize candidate batches. Path convergence and finite termination are stated under explicit regularity conditions. Finally, the day-ahead implementation and settlement boundaries are clarified. The analytical active-set radius, critical carbon value, and closed-loop gain remain diagnostic quantities and are not required by the main algorithm.

4.1. Batch Selection and Ordered-Path Discretization Under a Limited Re-Clearing Budget

Fractions of a fixed-composition population are admitted in a prescribed sequence of batches, and each admitted fraction submits one final response based on the signal available at its admission. Previously admitted aggregators do not repeatedly revise their schedules after subsequent signal updates. The total responsive population is normalized to one, and $p \in [0, 1]$ denotes the cumulative participation fraction.

Let $f^{\delta_m}(D)$ be the nodal–temporal load increment produced by one unit of the responsive population under the finite-difference electricity–carbon signal $s^{\delta_m}(D)$:

$$f^{\delta_m}(D) = \sum_i P_i X_i\Big(s_i^{\delta_m}(D)\Big), \tag{50}$$

where X_i is the aggregator response defined in Section 2.3, and P_i embeds the response of aggregator i into the system demand coordinates.

Here, $f^{\delta_m}(D)$ denotes the aggregate response of a unit fraction of a population with fixed composition. Every admitted fraction contains the same proportions of all modeled industrial, commercial, and residential aggregators; these composition weights are held constant across the participation coordinate p and batch index g and are suppressed from the notation. Accordingly, f^{δ_m} depends only on D under the participation model studied here. The prescribed order refers to the sequence of batch updates, not to an arbitrary arrival order of individual heterogeneous aggregators.

If the population is infinitesimally divided and the market is re-cleared after every infinitesimal admission, the ordered participation path satisfies

$$\frac{\mathrm{d}D(p)}{\mathrm{d}p} = f^{\delta_m}(D(p)), \qquad D(0) = D^0, \qquad p \in [0, 1]. \tag{51}$$

The endpoint $D(1)$ represents a sequential process in which every user responds once in the prescribed order. It is generally different from an autonomous fixed point obtained by repeatedly allowing all users to revise their schedules.

In practice, Equation (51) must be discretized into a finite number of batches. Let $p_{\mathrm{rem},g}$ be the remaining population fraction before batch g, and let γ_g be the fraction selected from that remaining population. The corresponding fraction of the total population is

$$\omega_g = p_{\mathrm{rem},g}\gamma_g. \tag{52}$$

For a candidate batch g, the coarse endpoint is computed for the acceptance comparison. If the candidate is accepted, the demand state is advanced through two half steps, with re-clearing at the midpoint:

$$\begin{aligned} \widehat{D}^{(g)} &= D^{(g-1)} + \omega_g f^{\delta_m}\big(D^{(g-1)}\big), \\ D^{(g)}_{\mathrm{mid}} &= D^{(g-1)} + \frac{\omega_g}{2} f^{\delta_m}\big(D^{(g-1)}\big), \\ D^{(g)} &= D^{(g)}_{\mathrm{mid}} + \frac{\omega_g}{2} f^{\delta_m}\big(D^{(g)}_{\mathrm{mid}}\big). \end{aligned} \tag{53}$$

In the adaptive method, an accepted macro step indexed by g has total participation size ω_g and is implemented as two half-step user batches, each of size $\omega_g/2$, with a market re-clearing at the midpoint. Accordingly, we report the number of accepted macro steps and the number of accepted half-step user batches separately; the latter is twice the former. In the fixed benchmark, G denotes the prescribed number of fixed groups.

The remaining population is updated as

$$p_{\mathrm{rem},g+1} = p_{\mathrm{rem},g}(1 - \gamma_g), \qquad p_{\mathrm{rem},1} = 1. \tag{54}$$

In Equation (53), $\widehat{D}^{(g)}$ is an auxiliary coarse endpoint used only for the acceptance comparison; $D^{(g)}$ is the accepted endpoint propagated to the next batch. The two accepted half steps constitute an explicit Euler discretization of Equation (51). Complete allocation requires

$$p_{\mathrm{rem},G+1} = 0, \qquad \sum_{g=1}^{G} \omega_g = 1. \tag{55}$$

Equal division into G fixed batches is recovered by setting

$$\gamma_g = \frac{1}{G-g+1}, \tag{56}$$

which yields

$$\omega_g = \frac{1}{G}, \qquad g = 1, \ldots, G. \tag{57}$$

A small G may allow one batch to cross several market critical regions, leaving subsequent users exposed to a stale signal. A large G may consume many SCED solves while providing little additional endpoint accuracy. Because the appropriate G changes with participation scale and market conditions, no fixed grouping can be expected to balance accuracy and computational effort ex ante.

Denote a batch policy by

$$\Pi = \left\{\omega_g,\, D^{(g)},\, a_g\right\}_{g=1}^{G}, \tag{58}$$

where $a_g \in \{0,1\}$ indicates whether candidate batch g is accepted. Let $N_{\mathrm{SCED}}(\Pi)$ be the total number of SCED solves required by Π, including baseline clearing, finite-difference signal evaluations, midpoint re-clearing, rejected trials, and endpoint verification. Given an available budget B, the batch-selection problem is

$$\begin{aligned} \min_{\Pi} \quad & \left\| D_{\Pi}^{\mathrm{end}} - D_{\mathrm{ref}} \right\|_2 \\ \text{s.t.} \quad & N_{\mathrm{SCED}}(\Pi) \le B, \\ & \omega_g > 0, \qquad \sum_{g=1}^{G} \omega_g = 1, \\ & D^{(g)} = \Psi_{\omega_g}\left(D^{(g-1)}\right), \qquad g = 1, \ldots, G. \end{aligned} \tag{59}$$

Here, $D_{\Pi}^{\mathrm{end}} = D^{(G)}$ is the policy endpoint, and D_{ref} is a numerical approximation of the continuous ordered-path endpoint under the same participation order. In the numerical study, D_{ref} is obtained through constrained Richardson extrapolation of the 64-, 128-, and 256-batch paths. It is used only for ex post-accuracy assessment and is unavailable to the online policy.

The primary objective in Equation (59) is endpoint accuracy under a given SCED budget. Realized emissions, operating cost, and emission deviations from the reference path are reported as physical outcomes. They do not define competing method rankings.

Problem (59) is an online sequential decision problem. The reference endpoint and future active-set transitions are unknown during operation. The proposed method therefore does not claim to solve the global policy optimization exactly. It uses the locally observed coarse–fine discrepancy to allocate re-clearing effort along the realized path.

4.2. One-Step–Two-Half-Step Error Estimate and Acceptance Rule

Consider a candidate participation fraction ω at the current state D. Applying the entire candidate population under the current static signal gives the coarse endpoint

$$\Phi_{\omega}(D) = D + \omega f^{\delta_m}(D). \tag{60}$$

The same total population is then divided into two half batches. The first half produces the midpoint

$$D^{1/2} = \Phi_{\omega/2}(D) = D + \frac{\omega}{2} f^{\delta_m}(D). \tag{61}$$

The SCED problem and electricity–carbon signal are recomputed at $D^{1/2}$ before admitting the second half. The fine endpoint is

$$\begin{aligned} \Psi_\omega(D) &= \Phi_{\omega/2}\big(\Phi_{\omega/2}(D)\big) \\ &= D + \frac{\omega}{2} f^{\delta_m}(D) + \frac{\omega}{2} f^{\delta_m}\Big(D + \frac{\omega}{2} f^{\delta_m}(D)\Big). \end{aligned} \tag{62}$$

The directly observable coarse–fine difference is

$$e_\omega(D) = \|\Psi_\omega(D) - \Phi_\omega(D)\|_2. \tag{63}$$

This quantity compares a within-batch static signal with one midpoint signal update for the same participation fraction. It is obtained from candidate re-clearing outcomes and does not require the full market Jacobian, an analytical active-set radius, or a closed-loop spectral gain.

For a prescribed threshold $\tau_D > 0$, the candidate is accepted if and only if

$$\text{accept}(\omega) \iff e_\omega(D) \le \tau_D. \tag{64}$$

For batch g, the coarse endpoint $\Phi_{\omega_g}(D^{(g-1)})$ is the auxiliary endpoint $\widehat{D}^{(g)}$ in Equation (53), whereas the fine endpoint $\Psi_{\omega_g}(D^{(g-1)})$ is the accepted state $D^{(g)}$. Only $D^{(g)}$ is propagated to the next batch.

An accepted candidate adopts the fine endpoint

$$D_{\text{new}} = \Psi_\omega(D). \tag{65}$$

If $e_\omega(D) > \tau_D$, the trial is rejected and the last accepted state is retained:

$$D_{\text{new}} = D. \tag{66}$$

A rejection rolls back only the candidate calculation conducted during day-ahead scheduling. It does not reverse an implemented physical response.

Because the coarse–fine difference is second order in a smooth region, the next candidate fraction is adjusted by a square-root controller:

$$\omega_{\text{new}} = \text{clip}_{[\omega_{\min}, \omega_{\max}]}\left\{\beta\omega\left[\frac{\tau_D}{\max(e_\omega, \varepsilon)}\right]^{1/2}\right\}, \tag{67}$$

where $\beta \in (0, 1]$ is a safety factor, $\varepsilon > 0$ prevents division by zero, and the clipping operator enforces the admissible range.

Accepted and rejected trials use different multiplier intervals:

$$\omega_{\text{new}} = \min\{p_{\text{rem}}, \rho\omega\}, \tag{68}$$

$$\rho = \begin{cases} \text{clip}_{[\rho^-_{\text{acc}}, \rho^+_{\text{acc}}]}\left\{\beta\left[\dfrac{\tau_D}{\max(e_\omega, \varepsilon)}\right]^{1/2}\right\}, & e_\omega \le \tau_D, \\ \text{clip}_{[\rho^-_{\text{rej}}, \rho^+_{\text{rej}}]}\left\{\beta\left[\dfrac{\tau_D}{\max(e_\omega, \varepsilon)}\right]^{1/2}\right\}, & e_\omega > \tau_D. \end{cases} \tag{69}$$

The rejection multipliers satisfy

$$0 < \rho^-_{\text{rej}} \le \rho^+_{\text{rej}} < 1, \tag{70}$$

ensuring that a rejected candidate is strictly reduced. An accepted step may expand when the observed discrepancy is sufficiently below the threshold.

Proposition 4 (Local step-doubling relation)**.** *Suppose that f^{δ_m} is twice continuously differentiable in the current critical region and that the coarse step and both half steps remain in that region. Then*

$$\Psi_\omega(D) - \Phi_\omega(D) = \frac{\omega^2}{4} J_{f^{\delta_m}}(D) f^{\delta_m}(D) + O(\omega^3). \tag{71}$$

Consequently,

$$e_\omega(D) = \frac{\omega^2}{4} \left\| J_{f^{\delta_m}}(D) f^{\delta_m}(D) \right\|_2 + O(\omega^3). \tag{72}$$

A first-order expansion of the second half-step response gives

$$f^{\delta_m}\left(D + \frac{\omega}{2} f^{\delta_m}(D)\right) = f^{\delta_m}(D) + \frac{\omega}{2} J_{f^{\delta_m}}(D) f^{\delta_m}(D) + O(\omega^2), \tag{73}$$

which yields Equation (71). The complete proof is provided in Appendix A.

Proposition 4 explains the exponent 1/2 in Equation (67). In a smooth region, moving the observed difference towards τ_D requires approximately

$$\omega_{\text{new}} \approx \omega \left(\frac{\tau_D}{e_\omega} \right)^{1/2}. \tag{74}$$

The asymptotic relation is not guaranteed when either path crosses a market or user active-set boundary. Errors from different affine regions may partially cancel, resulting in a small e_ω despite a non-negligible endpoint error. Accordingly, τ_D is a coarse–fine difference threshold rather than a global error budget or an accuracy certificate. Endpoint accuracy is assessed independently against refined reference paths.

4.3. Convergence and Finite Termination

This subsection states the two main analytical properties of the method. Detailed proofs are deferred to the Appendix B.

Let the continuous ordered path and all Euler iterates remain in a compact convex set $\mathcal{K}$. Assume that the finite-difference signal is single valued and that each aggregator problem has a unique solution. The resulting vector field $f^{\delta_m} = X \circ s^{\delta_m}$ is assumed to satisfy

$$\left\| f^{\delta_m}(D_1) - f^{\delta_m}(D_2) \right\|_2 \le L_f \|D_1 - D_2\|_2, \qquad D_1, D_2 \in \mathcal{K}, \tag{75}$$

and

$$F_f = \sup_{D \in \mathcal{K}} \left\| f^{\delta_m}(D) \right\|_2 < \infty. \tag{76}$$

For accepted population fractions satisfying $\sum_{g=1}^{G} \omega_g = 1$, define

$$h = \max_{1 \le g \le G} \omega_g. \tag{77}$$

Theorem 1 (Convergence of the accepted participation path)**.** *Suppose that f^{δ_m} is L_f-Lipschitz on a convex set $\mathcal{K}$ containing the continuous path, all accepted endpoints, and all accepted half-step states. Suppose also that $\|f^{\delta_m}(D)\|_2 \le F_f$ for all $D \in \mathcal{K}$. If the accepted batches complete participation, $\sum_{g=1}^{G} \omega_g = 1$, and $h = \max_{1 \le g \le G} \omega_g$, then the endpoint $D^{(G)}$ generated by the accepted two-half-step update in Equation (53) satisfies*

$$\|D^{(G)} - D(1)\|_2 \le \frac{L_f F_f}{4} e^{L_f} h = O(h), \tag{78}$$

where $D(1)$ is the endpoint of the continuous participation path in Equation (51).

Proof sketch: Each accepted macro step ω_g consists of two explicit Euler substeps of length $\omega_g/2$. Applying the Euler error recurrence to this nonuniform substep grid bounds the endpoint error by $(L_f F_f/2)e^{L_f}$ times the sum of squared substep lengths. Since

$$\sum_{g=1}^{G} 2\left(\frac{\omega_g}{2}\right)^2 = \frac{1}{2}\sum_{g=1}^{G}\omega_g^2 \le \frac{h}{2}, \tag{79}$$

the stated bound follows. The complete proof is given in Appendix B.

The result applies to the ordered path generated by a fixed finite-difference step δ_m. It does not imply that smaller batches eliminate the finite-difference stencil bias. It also requires a single-valued signal selection. The present analysis and case studies hold batch composition fixed, as described in Section 3.1. If batch composition or arrival order is allowed to vary with the participation coordinate, the vector field must be written as $f(D, p)$, and the endpoint may depend on the participation order. Such heterogeneous arrival-order effects are outside the scope of this study.

Finite termination additionally requires a strictly positive minimum candidate fraction:

$$\omega_{\min} > 0. \tag{80}$$

Theorem 1 is a convergence result as the maximum accepted participation step h tends to zero under the stated assumptions. The acceptance condition based on the coarse–fine difference alone does not provide a global error certificate. A finite-group numerical reference is an approximation to $D(1)$, rather than the exact continuous-path endpoint.

Proposition 5 (Finite termination)**.** *Suppose that the remaining population is finite and that, at every candidate state visited by the algorithm,*

$$e_{\omega_{\min}}(D) \le \tau_D. \tag{81}$$

Then the complete population is allocated after at most

$$N_{\text{acc}} \le \left\lceil \frac{1}{\omega_{\min}} \right\rceil + 1 \tag{82}$$

accepted macro steps.

Because $\rho^{+}_{\text{rej}} < 1$, any rejected candidate larger than $\omega_{\min}$ reaches the minimum fraction after finitely many reductions. Condition (81) ensures that the minimum step is accepted. Each accepted step allocates at least $\omega_{\min}$, except possibly the final residual fraction.

If

$$e_{\omega_{\min}}(D) > \tau_D. \tag{83}$$

the threshold is unattainable under the specified minimum batch size. The algorithm terminates and reports the unallocated fraction rather than forcing an over-threshold terminal step. Similarly, if another candidate evaluation would result in

$$N_{\text{SCED}} > B, \tag{84}$$

the method reports an insufficient re-clearing budget instead of silently omitting a required signal update.

Theorem 1 establishes asymptotic path convergence as $h \to 0$, whereas Proposition 5 establishes finite completion for a fixed minimum batch size. Neither result converts the local threshold τ_D into a universal global endpoint-error bound. Numerical endpoint accuracy must still be evaluated using independently refined reference paths.

4.4. Implementation Procedure and Settlement Boundary

The convergence and termination properties established above justify the following day-ahead implementation procedure. The proposed method operates during day-ahead schedule formation. The system operator or an authorized coordination platform first clears the baseline market and publishes the energy LMP and finite-difference LMCE. Aggregators are subsequently admitted in batches. After each accepted batch, its schedule is incorporated into the demand parameter and the market is re-cleared before signals are released to the remaining population.

The procedure consists of five steps.

1. Initialization: Set the baseline demand D^0, remaining fraction $p_{\text{rem}} = 1$, initial candidate fraction ω, coarse–fine threshold τ_D, minimum fraction $\omega_{\min}$, and SCED budget B.
2. Current-state clearing: Solve the multi-period SCED problem at the last accepted state D, and evaluate $s^{\delta_m}(D)$ and $f^{\delta_m}(D)$.
3. Candidate coarse and fine evaluations: Compute $\Phi_\omega(D)$ using Equation (60). Divide the same population fraction into two half batches, re-clear at the midpoint, and compute $\Psi_\omega(D)$ using Equation (62).
4. Acceptance or rejection: Evaluate e_ω from Equation (63). If $e_\omega \le \tau_D$, accept the fine endpoint, deduct the admitted population, and update the next candidate fraction. Otherwise, discard the trial, retain the last accepted state, and retry with a smaller ω.
5. Termination and reporting: When $p_{\text{rem}} = 0$, report the final demand, operating cost, emissions, shifted energy, accepted batches, rejected trials, SCED solves, and wall-clock time. If the minimum step violates the threshold or the remaining SCED budget is insufficient, terminate and report the unmet condition.

The state transition is summarized by

$$(D, p_{\text{rem}}) \leftarrow \begin{cases} \big(\Psi_\omega(D),\, p_{\text{rem}} - \omega\big), & e_\omega(D) \le \tau_D, \\ \big(D,\, p_{\text{rem}}\big), & e_\omega(D) > \tau_D. \end{cases} \tag{85}$$

The candidate fraction always satisfies

$$0 < \omega \le \min\{\omega_{\max}, p_{\text{rem}}\}. \tag{86}$$

Rejection and rollback occur only in the day-ahead computational environment. The candidate schedule has not yet become a physical dispatch instruction. Restoring the last accepted computational state therefore does not require any physical demand reversal. Previously admitted users retain their accepted schedules, and updated signals are released only to users who have not yet participated.

This mechanism differs from a real-time autonomous iteration. The problem concerns the locations and sizes of re-clearing batches along an ordered one-time participation process, rather than repeated user revisions towards a fixed point. All baseline, perturbation, midpoint, trial, and endpoint solves are included in N_{SCED}.

The additional demand-side carbon value μ_a may represent an internal carbon-budget shadow value, a low-carbon incentive, or a regulatory parameter. It is not an endogenous settlement price produced by the batching algorithm. If market clearing already internalizes the carbon component $\bar{\mu}E$, consistency requires

$$\mu_a = \mu_{\text{total}} - \bar{\mu} \tag{87}$$

to avoid double counting.

In summary, the proposed day-ahead procedure admits responsive demand in ordered batches, uses the coarse–fine difference to accept or reject each candidate batch, and terminates explicitly when the prescribed threshold or the remaining SCED budget cannot

be satisfied. The settlement-related role of μ_a is limited to avoiding carbon value double counting. Broader requirements concerning compensation, individual participation, data access, and operational compliance are discussed together with the method's applicability boundaries in Section 5.5.

5. Case Studies

This section evaluates the proposed error-estimate-driven batch-updating method from five complementary perspectives. First, the test system and numerical settings are introduced. Second, the endogenous failure of static electricity–carbon signals is verified using price–carbon mismatch, critical carbon values, active-set changes, and finite-difference diagnostics. Third, the relationship among batch selection, the SCED re-clearing budget, and endpoint accuracy is examined across different participation scales. Fourth, sensitivity analyses are conducted for renewable penetration, transmission capacity, storage flexibility, and renewable-generation uncertainty. Finally, the applicability boundaries and engineering implementation requirements of the proposed method are discussed separately.

5.1. Test System and Parameter Settings

The numerical experiments are conducted on a modified IEEE 14-bus system over a 24 h scheduling horizon. The system contains five conventional generating units with heterogeneous operating costs and emission factors. Wind farms with rated capacities of 100 and 80 MW are connected to buses 3 and 6, respectively, whereas photovoltaic plants with rated capacities of 80 and 50 MW are connected to buses 9 and 14. The baseline renewable-capacity scale is set to 0.65.

Flexible demand is located at buses 3, 4, 9, and 14. These buses are assigned synthetic industrial, commercial, commercial, and residential aggregator types, respectively, to represent heterogeneous response limits and discomfort coefficients. These labels are introduced for the present case study and are not native attributes of the standard IEEE 14-bus data set. In each participation batch, the same scaling factor is applied to the flexible demand at all four buses. Thus, every admitted fraction preserves the same proportional composition of industrial, commercial, and residential aggregators; the batches differ only in the sequence of signal updates, not in the order in which individual aggregators arrive.

The source of the base network data, the applied modifications, and the coefficients and construction rules for the 24 h nodal-demand and renewable-availability inputs are provided in Appendix C.

The main test-system settings are summarized in Table 2. Appendix C provides additional numerical specifications, including selected test-system modifications, generator cost and emission parameters, demand-response settings, and adaptive-controller and SCED solver settings.

Two model layers are used to separate the underlying mechanism from the intertemporal implementation. The first layer consists of 24 hourly DC-SCED problems without ramping, reserve, or storage state-of-charge coupling. Its market-signal Jacobian is block diagonal and is used to isolate price–carbon mismatch, active-set transitions, and participation-scale effects. The second layer is a fully coupled 24 h formulation incorporating generator ramping limits, spinning reserve requirements, and the state-of-charge dynamics of a storage unit at bus 9. This layer is used for the primary batch-updating and budget-accuracy experiments.

Because the time interval is $\Delta t = 1$ h, an hourly demand adjustment expressed in MW is numerically equal to its energy contribution in MWh. Accordingly, path lengths and endpoint errors over the complete horizon are reported in MWh. The major numerical settings are summarized in Table 2.

The participation scale is stated separately for each numerical experiment. The budget-accuracy comparison in Table 3 considers 1×, 2×, 3×, 5×, and 8× participation. The diagnostic experiments use the scale specified in the corresponding subsection, table, or figure caption.

Table 2. Main settings of the test system.

Item	Setting
Market model	24 h DC-SCED with nodal power balance and transmission constraints
Conventional generation	Five units with heterogeneous quadratic costs and emission factors
Renewable generation	Wind at buses 3 and 6; photovoltaic generation at buses 9 and 14
Responsive buses	Buses 3, 4, 9, and 14
Critical transmission element	Line 20 capacity set to 0.24 times its synthetic-data rating
Additional carbon value	$\mu_a = 180$ CNY/tCO$_2$
LMCE perturbation	$\delta_m = 0.1$ MWh
Outer Jacobian perturbation	$\varepsilon_J = 0.1$ MWh
Reserve requirement	5% of system demand plus 15% of available renewable generation
Storage configuration	20 MW/60 MWh at bus 9, with charging and discharging efficiencies of 0.95
Main embedded threshold	$\tau_D = 2.00$ MWh
Threshold sensitivity	$\tau_D \in \{0.50, 1.00, 2.00\}$ MWh
Reference paths	Fixed 64-, 128-, and 256-group paths with constrained Richardson extrapolation
Participation scales	1×, 2×, 3×, 5×, and 8×

Table 3. Budget-matched endpoint accuracy and runtime across participation scales.

Scale	Adaptive (Batches/SCED/s)	Adaptive Error (MWh)	Best Fixed (G/SCED/s)	Fixed Error (MWh)	Error Gap ΔE (MWh)	Reference Error u_{ref} (MWh)
1×	6/686/109.14	0.951	4/389/61.96	1.183	−0.232	0.033
2×	8/979/155.56	1.313	8/777/123.31	1.162	+0.151	0.072
3×	14/1761/276.03	1.420	16/1553/247.11	1.577	−0.157	0.185
5×	20/2349/368.65	1.608	20/1941/308.29	1.806	−0.198	0.116
8×	30/3426/538.25	2.890	32/3105/491.57	2.285	+0.605	0.413

Note: Each method entry reports batches, SCED solves, and wall-clock time in seconds, in that order. ΔE is the adaptive endpoint error minus the fixed endpoint error; a negative value favors the adaptive method. u_{ref} is the estimated remaining error of the Richardson reference endpoint, not a rigorous error bound.

The modified IEEE 14-bus system was selected as a controlled proof-of-concept test bed rather than as a scale estimate for a target urban network. It combines five conventional generators, two wind farms, two photovoltaic plants, flexible demand at four buses representing three aggregator types, a constrained transmission element, and storage. In particular, the capacity of line 20 is reduced to 0.24 times its input rating. These features allow us to examine price–carbon mismatch, changes in market active sets, intertemporal operating constraints, and demand-response feedback, while keeping the repeated 24 h SCED calculations computationally manageable. The selected system size therefore reflects a balance between representing the mechanisms studied and the computational requirements of repeated market re-clearing.

The consistency of the operating-cost path calculation is checked by perturbing eight bus-hour coordinates by 0.001 MWh. The maximum absolute difference between the analytical and finite-difference market-objective gradients is 2.77×10^{-4} CNY/MWh. After removing the carbon-cost component embedded in the supply-side objective, the maximum physical-cost-gradient error remains below 2.77×10^{-4} CNY/MWh.

Figure 1 illustrates the intertemporal nature of the extended system. Both the LMP and LMCE at bus 9 vary substantially over the scheduling horizon, while the storage unit shifts energy across hours according to the prevailing market conditions.

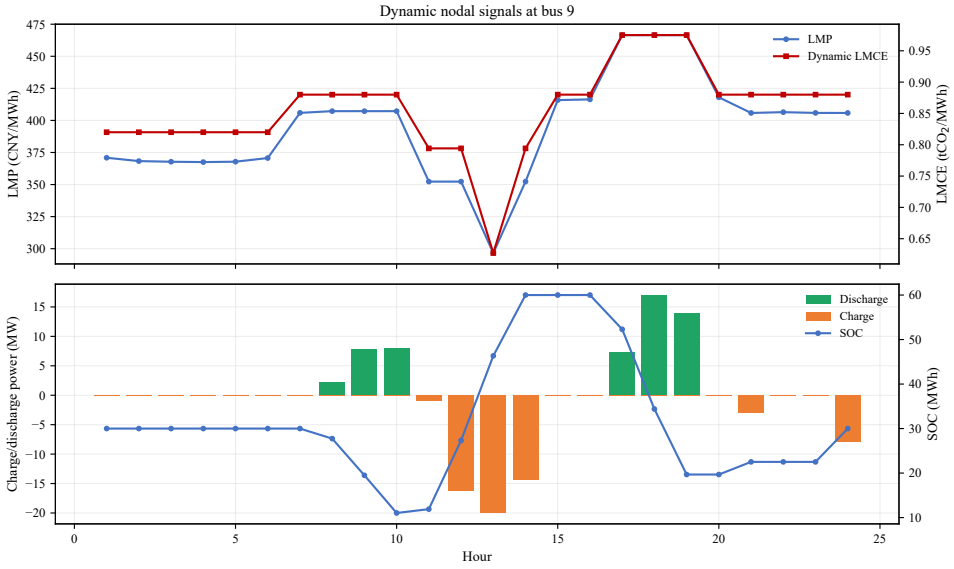


Figure 1. Dynamic nodal electricity–carbon signals and storage operation at bus 9.

5.2. Verification of Static-Signal Failure

5.2.1. Price–Carbon Mismatch and Carbon Rebound

Figure 2 shows the mismatch between the hourly LMP and LMCE rankings at the four responsive buses. The mismatch index ranges from approximately 18.5% to 22.8%, indicating that a lower electricity price does not necessarily correspond to a lower marginal emission rate. The exact ordering of the first three buses changes slightly with solver settings; therefore, the figure is used to establish the existence of the mismatch rather than to claim a universal spatial ranking.

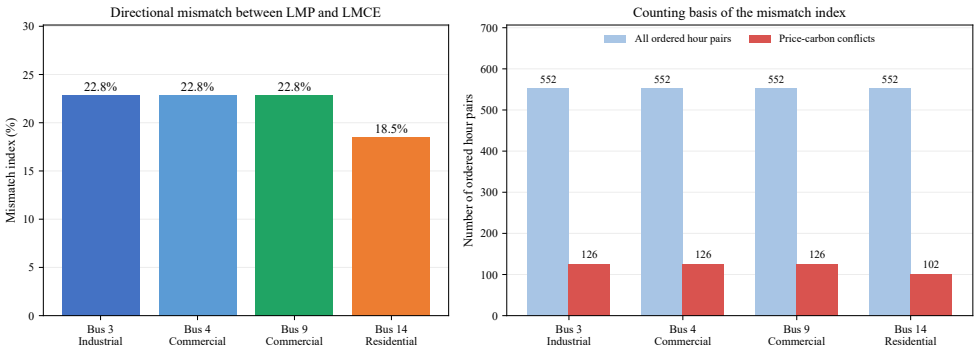


Figure 2. Directional mismatch between nodal electricity prices and marginal carbon signals.

At the 1× participation level, price-only response reduces the operating cost by 0.789% but increases carbon emissions by 7.83 tCO_2, corresponding to a 0.381% emission increase. This result directly demonstrates that an economically beneficial load shift can produce a carbon rebound when the temporal rankings of the electricity and carbon signals are inconsistent.

Introducing the LMCE into the demand-side signal changes the response direction. A static LMCE-only signal reduces emissions by 20.13 tCO_2 but increases the operating cost by 0.299%. The static composite signal produces a more balanced outcome, reducing the operating cost and emissions by 0.430% and 0.260%, respectively. At this relatively small participation level, four-batch updating changes the emission reduction only slightly, indicating that the static signal remains a reasonable approximation for marginal participation.

All numerical experiments were performed on the same workstation with 32 GB of RAM, using identical computational settings for the fixed and adaptive methods.

5.2.2. Critical Carbon Value and Active-Set Correction

The critical carbon value at which the composite signal changes from emission-increasing to emission-reducing depends strongly on whether response limits and market re-clearing are represented. Figure 3 compares three estimates.

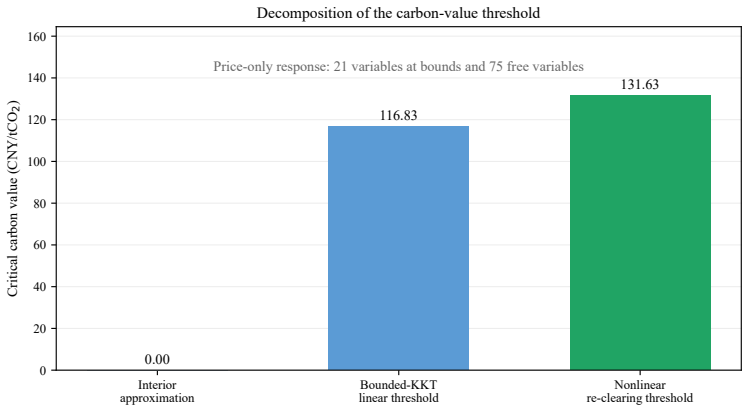


Figure 3. Critical carbon values obtained from the interior approximation, bounded-KKT model, and nonlinear market re-clearing.

When all demand-response variables are incorrectly assumed to be interior, the covariance-based approximation gives a critical value of zero. However, 21 of the 96 bus-hour response variables reach their upper or lower bounds in the price-only solution. Accounting for these active bounds through the KKT conditions raises the linear critical value to 116.83 CNY/tCO_2. Re-evaluating the response through nonlinear market re-clearing further increases the threshold to 131.63 CNY/tCO_2.

The difference between the latter two values arises because the bounded-KKT approximation corrects the feasible response direction but still retains the initial market sensitivity. Re-clearing additionally allows marginal generators, transmission constraints, and renewable curtailment states to change. The critical carbon value is therefore retained as an auxiliary diagnostic rather than being used in the proposed batch-size controller.

5.2.3. Participation-Scale-Induced Signal Distortion

Let ΔE_{lin} denote the emission change predicted using the static finite-difference LMCE, and let ΔE_{rc} denote the realized emission change obtained after market re-clearing. The static-signal residual and relative distortion are defined as

$$R_{\mathrm{stat}} = \Delta E_{\mathrm{rc}} - \Delta E_{\mathrm{lin}}, \qquad \eta_{\mathrm{stat}} = \frac{|R_{\mathrm{stat}}|}{\max(|\Delta E_{\mathrm{rc}}|, \epsilon_E)}, \tag{88}$$

where $\epsilon_E > 0$ prevents division by a near-zero realized change.

Figure 4 compares the static prediction with the re-cleared outcome as participation increases. At 0.5× participation, the static LMCE predicts a 3.44 tCO_2 emission reduction, whereas re-clearing realizes 2.82 tCO_2, giving $\eta_{\mathrm{stat}} = 22.2\%$. At 3×, the predicted and realized reductions are 20.67 and 9.30 tCO_2, respectively, and the relative distortion increases to 122.3%.

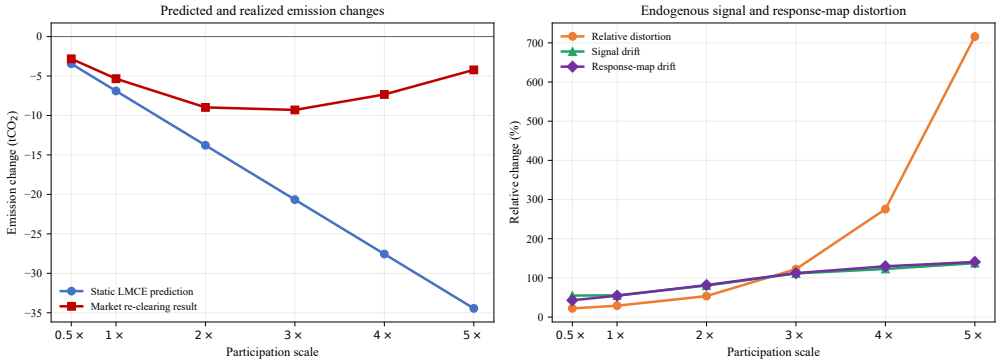


Figure 4. Static LMCE prediction, realized emission change, and endogenous signal distortion at different participation scales.

The discrepancy becomes particularly pronounced at 5× participation. The static LMCE predicts an emission reduction of 34.45 tCO_2, but re-clearing realizes only 4.22 tCO_2. Consequently, $R_{stat} = 30.22$ tCO_2 and $\eta_{stat} = 716.0\%$. The baseline and endpoint active-state signatures differ in 26 constraints. This value is an endpoint difference count and must not be interpreted as 26 sequential switching events along the path.

Over the same range, the relative drift of the de-meaned composite signal reaches 137.6%, while the directional response-map drift reaches 140.7%. These results indicate that the dominant error is not a failure of the aggregator to implement the prescribed response. Instead, the gradient used by later participants has become inconsistent with the endogenously altered market state.

The economic and carbon effects of this mechanism are shown in Figure 5. Between 3× and 5× participation, the shifted energy under the static composite signal increases from 153.66 to 256.11 MWh, whereas its emission reduction deteriorates from 0.453% to 0.205%. In contrast, four-batch updating shifts only 187.81 MWh at 5× participation but reduces the operating cost and emissions by 1.258% and 0.741%, respectively. The additional improvement is therefore produced by updated response directions rather than by a larger amount of shifted demand.

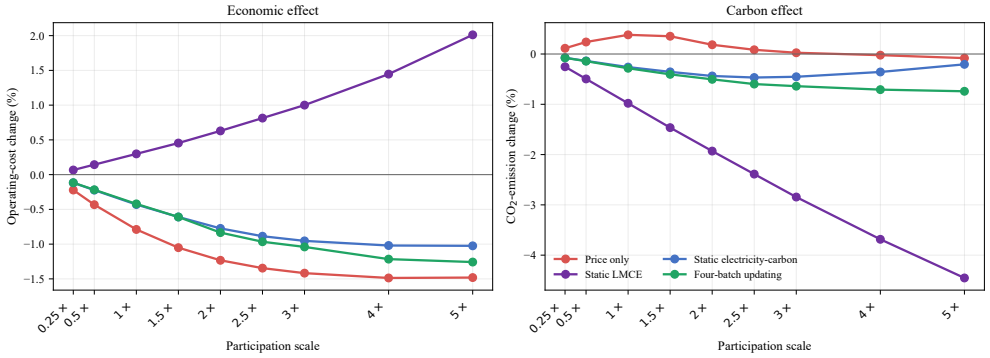


Figure 5. Economic and carbon effects of the response mechanisms as participation increases.

5.2.4. Numerical Safe-Side Radius and r_α

The analytical directional radius $\alpha_A(q)$ in Equation (35) requires the complete primal-dual sensitivity of all potentially binding market constraints. This quantity is not evaluated online and does not enter the proposed batch-size controller. For diagnostic purposes, the numerical implementation instead brackets the first active-state change observed along the planned response direction.

For each participation scale, the unit response direction is defined as

$$q = \frac{\Delta D}{\|\Delta D\|_2}, \qquad \|q\|_2 = 1, \tag{89}$$

and the market is repeatedly re-cleared along

$$D(\alpha) = D^0 + \alpha q. \tag{90}$$

At each tested displacement, an active-state signature is constructed from the binding status of generator limits, renewable-generation limits, transmission constraints, reserve constraints, ramping constraints, load shedding, voltage-angle limits, and storage variables, where applicable. A finite directional scan first identifies two consecutive displacements with different active-state signatures. Bisection is then applied to obtain

$$\alpha^-(q) \le \alpha_{\mathcal{A}}^{\mathrm{num}}(q) \le \alpha^+(q), \tag{91}$$

where $\alpha^-(q)$ is the largest tested displacement that retains the baseline active-state signature and $\alpha^+(q)$ is the smallest tested displacement at which a changed signature is observed. The resulting bracket width is

$$\Delta\alpha_{\mathcal{A}} = \alpha^+(q) - \alpha^-(q). \tag{92}$$

Because the active-state signature depends on the solver feasibility tolerance and the prescribed binding tolerance, the bracket in Equation (91) is not an analytical KKT radius. Only the tested safe-side value $\alpha^-(q)$ is retained for the subsequent numerical comparison.

The safe-side radius ratio r_α is defined in Equation (36). As shown in Figure 6, the planned response exceeds the numerically observed safe-side boundary even at the smallest tested participation level, and r_α increases rapidly with participation scale.

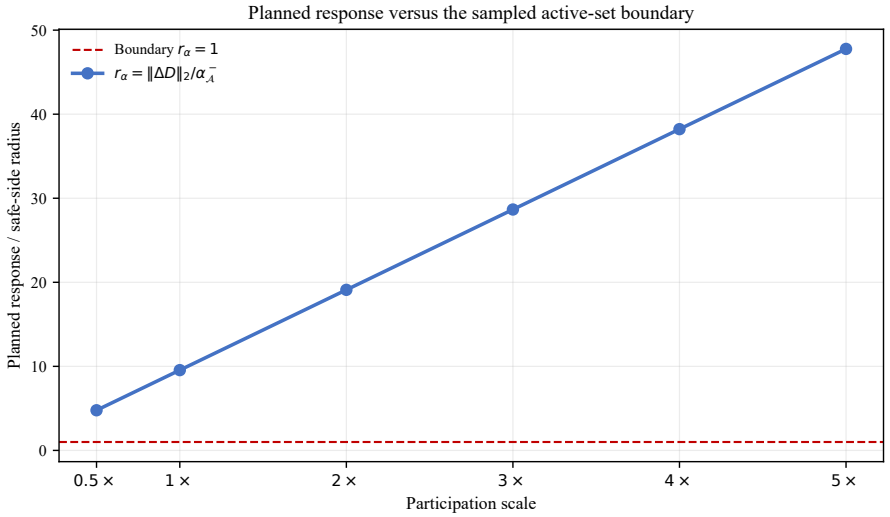


Figure 6. Ratio between the planned response and the numerically sampled safe-side active-set radius.

The condition $r_\alpha \ge 1$ means that the planned response has crossed the local safe-side boundary. It does not imply immediate deterioration in operating cost or emissions.

5.2.5. Closed-Loop Gain and Finite-Difference Step Separation

For the fully coupled intertemporal model, Figure 7 shows that the closed-loop gain Γ_2, defined in Equation (46), increases from approximately 0.030 at 0.5× participation to 0.300 at 5× participation but remains below unity.

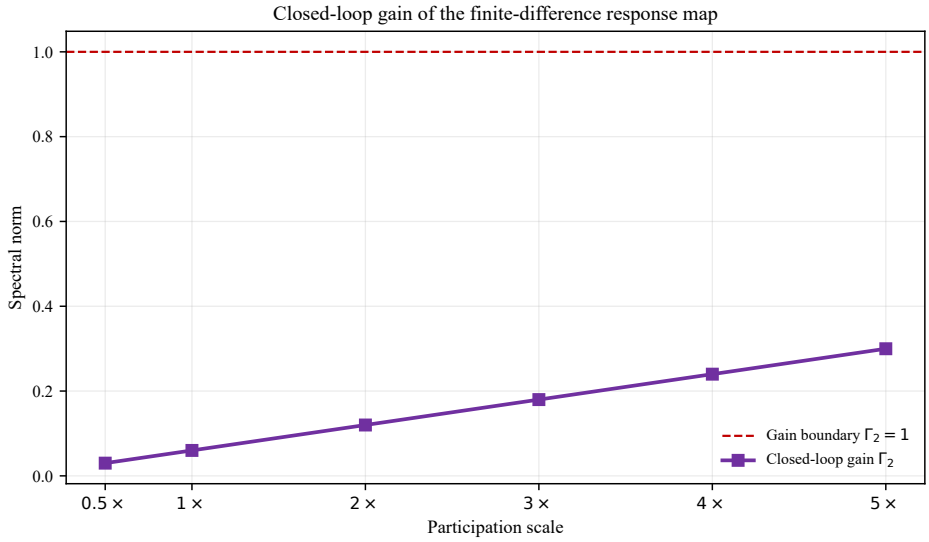


Figure 7. Closed-loop spectral gain of the finite-difference signal-response map.

The two diagnostics provide complementary evidence. The planned response crosses the numerically observed local boundary at an early stage, as indicated by $r_\alpha \geq 1$, whereas $\Gamma_2 < 1$ shows that the tested system does not exhibit local first-order amplification. Nevertheless, the static-signal residual continues to accumulate across successive active-set regions. Therefore, local non-expansiveness does not guarantee the long-range validity of a static signal.

Separate perturbation tests show that the inner LMCE step and the outer Jacobian step have only minor effects within the practical numerical range. To reduce the possibility that the directional probe itself crosses the observed boundary, its step is restricted by $\varepsilon_J \leq 0.5\alpha^-(q)$.

The quantities $\alpha^-(q)$, r_α, and Γ_2 are auxiliary diagnostics only. Candidate acceptance, rejection, and resizing are governed by the observable one-step–two-half-step difference e_ω and its prescribed threshold τ_D.

5.3. Budget-Accuracy Verification of Error-Estimate-Driven Updating

5.3.1. Adaptive Path and Acceptance Behavior

For each candidate macro step of normalized size ω, the method compares one coarse step with two re-cleared half steps. The observed coarse–fine difference is

$$e_\omega = \|\Psi_\omega(D) - \Phi_\omega(D)\|_2, \tag{93}$$

and the candidate is accepted when

$$e_\omega \leq \tau_D. \tag{94}$$

The accepted state is the endpoint obtained from the two half steps.

At the 5× participation level and $\tau_D = 2.00$ MWh, the algorithm accepts 10 macro steps, corresponding to 20 user batches. Figure 8 shows that the batch sizes are nonuniform. The controller reduces the next step when the observed difference approaches the threshold and enlarges it when the estimated local nonlinearity is small.

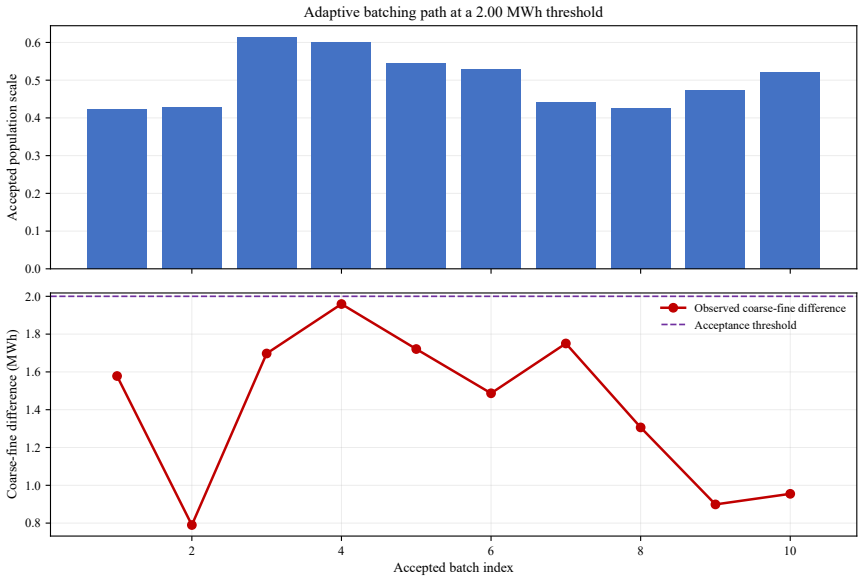


Figure 8. Accepted macro steps and observed coarse–fine differences at a 2.00 MWh threshold.

Decreasing τ_D from 2.00 to 1.00 and 0.50 MWh increases the number of accepted batches from 20 to 40 and 68, respectively. As shown in Figure 9, the final operating-cost and emission outcomes vary only slightly across the three thresholds, whereas the computational burden changes substantially.

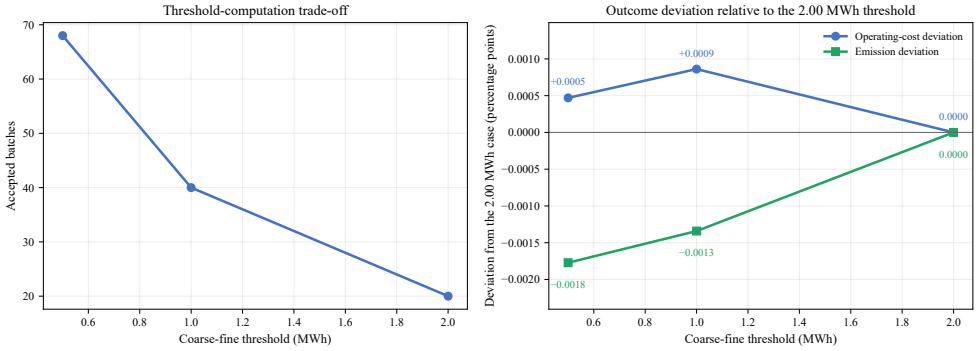


Figure 9. Effects of the coarse–fine threshold on the accepted batch count and final outcomes.

At $\tau_D = 2.00$ MWh, the adaptive method requires 2349 SCED solves and produces cost and emission changes of −1.034% and −0.705%, respectively. A fixed 20-group method requires 1941 solves and yields −1.035% and −0.705%. The near-identical operating outcomes show that the main contribution of adaptive batching is not guaranteed superiority over an ex post selected fixed grouping at one particular scale. Its value lies in selecting the update locations without prior knowledge of the appropriate fixed group count.

5.3.2. Reference-Path Convergence

The endpoint error of method Π is evaluated as

$$\epsilon_D(\Pi) = \left\| D_{\Pi}^{\text{end}} - D_{\text{ref}} \right\|_2, \tag{95}$$

where D_{ref} is constructed from the 64-, 128-, and 256-group paths using constrained Richardson extrapolation.

Figure 10 shows the refinement differences. At participation scales of 2×, 3×, 5×, and 8×, the 128-to-256-group difference is smaller than the 64-to-128-group difference. At 1×,

however, the difference increases slightly from 0.030 to 0.033 MWh. Therefore, the 256-group solution is not treated as exact ground truth.

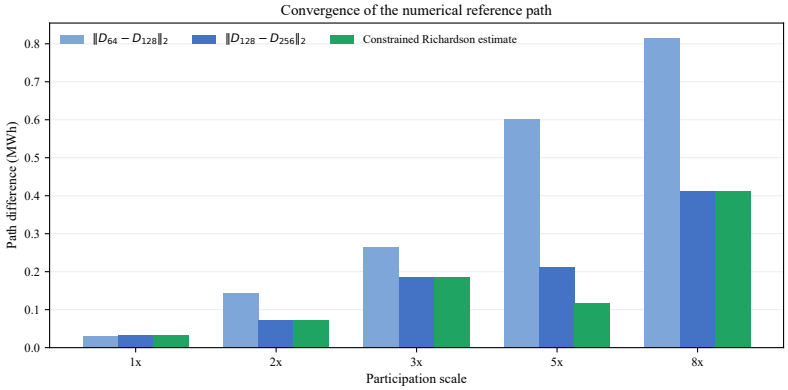


Figure 10. Refinement differences and constrained Richardson estimates of the numerical reference path.

The constrained effective order is defined by

$$p_{\text{eff}} = \max(p_{\text{obs}}, 1), \tag{96}$$

so that nonmonotone or nonpositive observed orders revert to a conservative first-order correction. The maximum estimated remaining reference error over the five participation scales is 0.413 MWh. This uncertainty is retained when interpreting differences between the adaptive and fixed schemes.

5.3.3. Cross-Scale Necessity of Adaptive Batching

Figure 11 compares endpoint accuracy under the realized SCED budget of the adaptive method. For each participation scale, the fixed comparator is restricted to schemes whose SCED solve count does not exceed the adaptive budget.

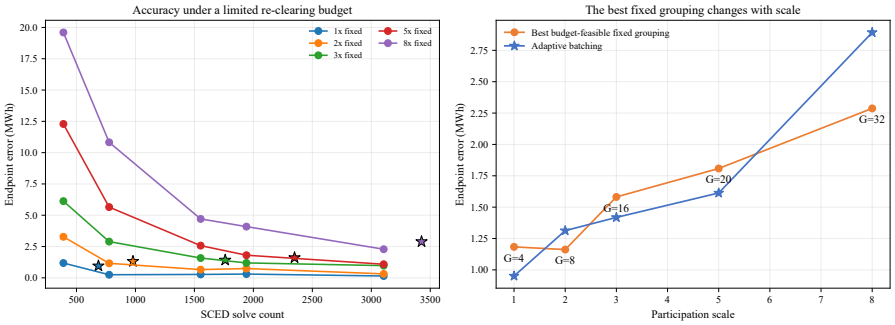


Figure 11. SCED budget and endpoint accuracy across participation scales. Stars denote adaptive results.

The results are summarized in Table 3. The best budget-feasible fixed group count changes from 4 to 8, 16, 20, and 32 as the participation scale increases. By contrast, the adaptive method automatically forms 6, 8, 14, 20, and 30 batches.

The estimated reference-path errors at participation scales of 1, 2, 3, 5, and 8 are 0.033, 0.072, 0.185, 0.116, and 0.413 MWh, respectively. The signed differences between the adaptive and budget-feasible best fixed endpoint errors are −0.232, +0.151, −0.157, −0.198, and +0.605 MWh, where a negative value favors the adaptive method. Because each method error is measured relative to the same estimated reference endpoint, we use $2u_{\text{ref}}$ as a conservative diagnostic scale for interpreting their difference; this comparison is not a formal uncertainty bound. The adaptive advantage at the 1× scale is clearly larger

than this diagnostic scale. The comparison at 2× is marginal, while the method ranking at 3×, 5×, and 8× is unresolved relative to the estimated reference uncertainty. Accordingly, these results do not establish a general accuracy advantage of adaptive batching over the budget-feasible best fixed grouping.

At the 5× participation scale, the adaptive method uses 2349 SCED solves and 368.65 s, compared with 1941 solves and 308.29 s for the fixed 20-group method. Thus, the adaptive method requires approximately 21.0% more SCED solves and 19.6% more wall-clock time at this operating point, while the operating-cost and emission outcomes are nearly identical: the differences are 5.66 CNY and 0.009 tCO_2, respectively. These results do not show a computational saving at every operating point. The practical role of the adaptive rule is to select batch sizes without requiring the operator to specify a fixed group count in advance.

These results support three conclusions. First, a single fixed group count is unsuitable over the complete participation range: 20 groups are excessive at small participation levels and insufficient at 8×. Second, the coarse–fine estimator increases the update frequency as the response path becomes more nonlinear. Third, the adaptive method tracks the budget-feasible fixed-grouping frontier without knowing the best fixed count in advance, although it does not dominate the ex post optimum at every scale.

5.4. Sensitivity, Storage, and Uncertainty Analyses

5.4.1. Renewable Penetration, Transmission Capacity, and Carbon-Cost Pass-Through

A combined sensitivity analysis is performed using four renewable-capacity scales, five line-20 capacity scales, and three carbon-cost pass-through factors, yielding 60 calculations. Carbon rebound is identified when price-based response reduces the operating cost but increases emissions.

As shown in Figure 12, 45 of the 60 calculations exhibit carbon rebound. However, the three carbon pass-through settings repeat the same 20 renewable-transmission structures. After removing these repetitions, rebound occurs in 15 of the 20 distinct structural combinations. This result is a grid count and must not be interpreted as an empirical probability.

Within the tested grid, renewable penetration is the primary factor determining the direction of the carbon effect. Price-based response increases emissions at renewable scales of 0.35, 0.50, and 0.65 for all tested line capacities. At a renewable scale of 0.80, the response becomes emission-reducing. Transmission capacity and carbon-cost pass-through modify the magnitude but do not change the sign within the selected parameter grid. These findings are conditional on the discrete scenarios and do not establish a universal causal ranking.

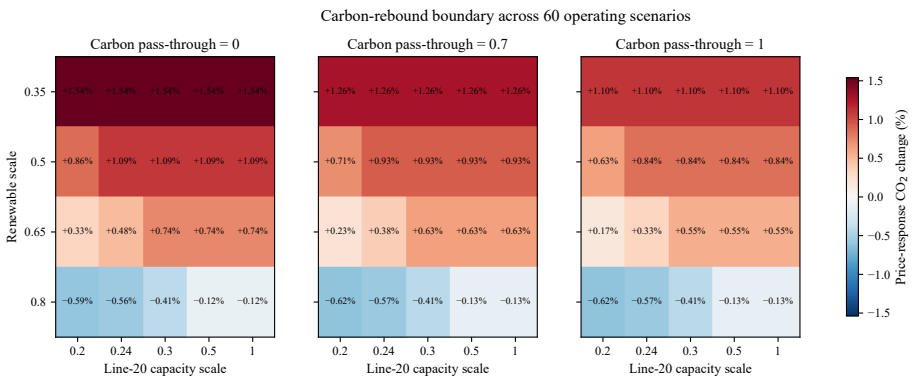


Figure 12. Carbon-rebound boundary under combined renewable, transmission-capacity, and carbon-cost-pass-through settings.

5.4.2. Storage Effects and Flexibility Substitution

Figure 13 shows the baseline influence of storage location. Storage reduces renewable curtailment but can increase system emissions when charging and discharging alter the marginal-generation schedule. Therefore, storage should not be classified as inherently low-carbon without considering its temporal operating pattern and location.

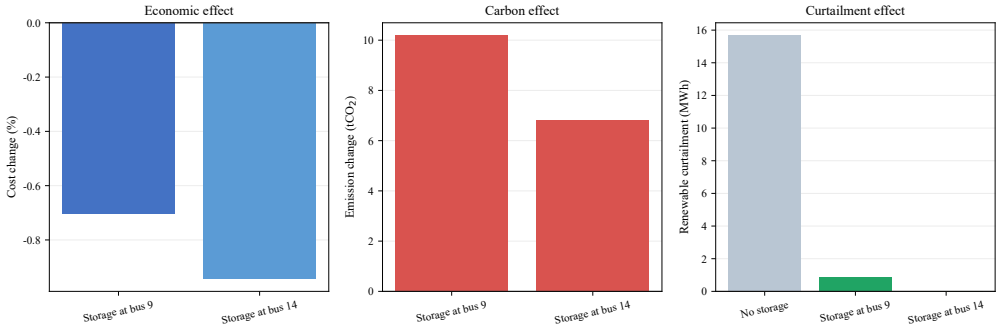


Figure 13. Effects of storage location on operating cost, emissions, and renewable curtailment.

Storage also changes the value of signal updating. Table 4 compares the static and four-batch composite-signal mechanisms at 3× participation.

Table 4. Interaction between storage flexibility and signal updating at 3× participation.

System Flexibility	Static Emission Change (%)	Batch Emission Change (%)	Static Cost Change (%)	Batch Cost Change (%)
No storage	−0.412	−0.662	−0.737	−1.049
Storage at bus 9	−0.562	−0.562	−0.853	−0.833
Storage at bus 14	−0.420	−0.404	−0.658	−0.606

Without storage, batch updating provides a clear improvement over the static signal. Storage at bus 9 absorbs most of the response-induced temporal imbalance, making the emission outcomes of the two mechanisms almost identical. With storage at bus 14, batch updating is slightly weaker than the static mechanism. Thus, storage and signal updating may be complementary or substitutive depending on their locations and the prevailing network constraints. Figure 14 illustrates these effects.

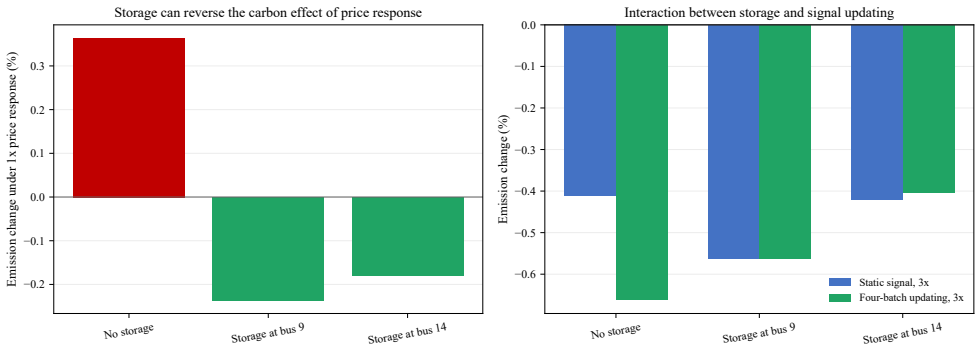


Figure 14. Interaction between storage configuration, price-response carbon effects, and signal updating.

Figure 15 further shows that demand response reduces the storage throughput and energy loss at bus 9, confirming that demand-side flexibility and storage flexibility may partially substitute for each other.

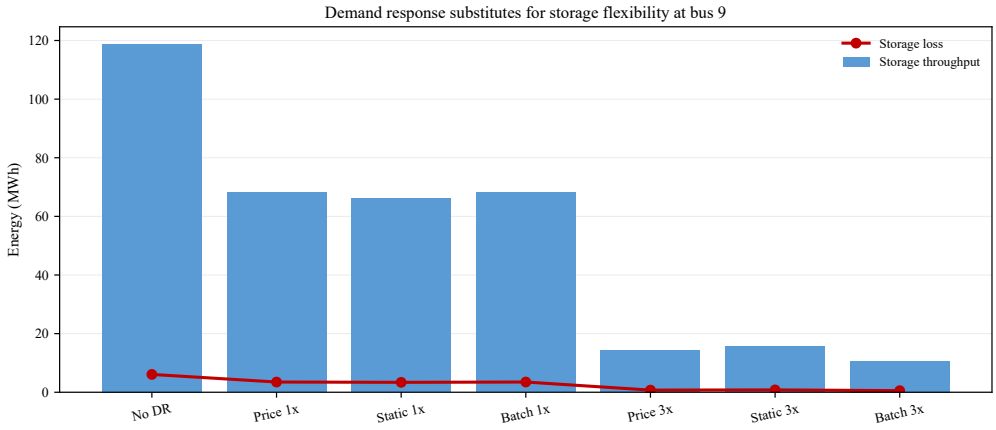


Figure 15. Substitution between demand response and storage flexibility at bus 9.

Finally, the influence of renewable-generation forecast errors on signal-release risk is examined as an engineering complement to the main analysis. The results indicate that local congestion and marginal-unit switching can spatially amplify forecast errors: the relative variability of the composite signal reaches 39.3% at bus 14. In the auxiliary experiment without adaptive batch updating, the scenario-mean scheme produces emission increases in 20.0% of the out-of-sample cases, whereas the interval-robust scheme reduces this frequency to 3.3%. No emission increase is observed for the conditional value-at-risk (CVaR)-based scheme in the 30 tested cases, although its expected operating cost increases by 0.717%. These results show that behavioral-feedback control and ex ante uncertainty management address different risks. Highly sensitive buses may require smaller response batches and more frequent signal updates, while robust signal construction is needed to limit forecast-induced scheduling risk.

In the present case, adaptive re-clearing is most useful at participation scales above 3×, when line 20 is congested and storage at bus 9 is unavailable. These conditions are associated with a greater need to adjust the batch size along the participation path, rather than to prespecify a single fixed group count. This is a case-specific finding: it does not imply that the adaptive method always requires fewer SCED solves or achieves a smaller endpoint error than an ex post selected fixed strategy.

5.5. Engineering Implementation and Applicability Boundaries

Practical implementation requires the system operator or an authorized coordination platform to access the SCED model or an equivalent iterative clearing interface. The platform must receive the accepted demand schedules, update the corresponding nodal demand parameters, perform midpoint and endpoint re-clearing, and release the updated signals to the remaining participants. These operations require consistent data-access permissions, communication deadlines, solver availability, and procedures for missing or non-compliant submissions.

Repeated SCED calculations are the main computational constraint of the proposed procedure. For each candidate fraction, the method evaluates the coarse endpoint and the fine endpoint obtained through two half steps, including a re-clearing at the midpoint. If a candidate is rejected, its trial calculations do not advance the accepted state and additional solves are required. Larger networks may increase the size and solution time of each SCED problem, although the increase depends on the network structure, model formulation, and solver. Practical deployment would therefore need to verify that the required re-clearings can be completed within the day-ahead clearing deadline, available computing resources,

and prescribed SCED budget. The present study demonstrates feasibility on a modified IEEE 14-bus system but does not establish computational scalability on larger systems.

The batching rule determines only the locations and sizes of signal updates. It does not determine aggregator compensation, benefit allocation, or individual participation constraints. An improvement in system operating cost or emissions does not imply that every participating aggregator is individually better off. A practical market design should therefore supplement the batching procedure with compensation rules, bill-impact limits, and individual-rationality constraints.

The storage results further show that signal updating and physical flexibility may be complementary or substitutive. When storage absorbs most of the response-induced temporal imbalance, the difference between static and updated signals becomes small.

Robust signal construction and adaptive batching address different sources of uncertainty. The former modifies the ex ante response plan to control forecast risk, whereas the latter allocates re-clearing effort along the participation path. They should therefore be treated as complementary rather than interchangeable mechanisms.

Accordingly, the present method should be interpreted as an operational coordination layer under a prescribed market model, response order, and SCED budget. It does not by itself constitute a complete settlement mechanism, a compensation-allocation rule, a stochastic market-clearing framework, or a source–network–load–storage investment-planning model.

Accordingly, the method is most applicable to day-ahead coordination settings in which each re-clearing result can be incorporated and communicated before the remaining participants respond, and in which the operator can allocate sufficient solver time and a defined SCED budget to the updates. Its practical value should therefore be assessed against the market-clearing deadline, available computing resources, and communication delays.

The reported case studies use the fixed-composition participation model specified in Section 3.1. If changes in the arrival sequence cause the type composition of admitted batches to vary with participation, the aggregate response field becomes sequence-dependent, as discussed after Theorem 1. Such changes may alter the demand path and the observed coarse–fine discrepancies, leading to different acceptance decisions, adaptive batch sizes, endpoint errors, and operating outcomes. The reported results should therefore be interpreted as applying to the specified fixed-composition model, rather than as predictions that are invariant to arbitrary heterogeneous arrival sequences. In practical applications, the composition of each admitted batch should be observed or estimated and incorporated into the response model. A systematic evaluation of alternative arrival sequences is left for future work.

Taken together, the case studies demonstrate that static electricity–carbon signals can become inaccurate because of endogenous market-state changes, even when local gain diagnostics remain below their nominal warning thresholds. Error-estimate-driven batching allocates a limited re-clearing budget without requiring a universally valid fixed group count. Its practical value is greatest when flexible-demand participation is large, network constraints are sensitive to the response path, and existing physical flexibility is insufficient to absorb the induced changes. The implementation requirements and limitations identified above delimit the scope within which these numerical benefits may be realized.

The modified IEEE 14-bus system and the specified demand, renewable-availability, and aggregator-response inputs provide a controlled setting for examining the proposed mechanism. Validation with calibrated network and operational data could change the timing and location of congestion, the marginal generators, and the intertemporal operating constraints. These changes could alter the magnitude of static-signal errors, the accepted batch sizes, the number of re-clearings, and the endpoint-accuracy comparisons; the direction of these changes cannot be inferred from the present simulations. In practice, response

delays, incomplete participation, measurement errors, and heterogeneous user behavior may also cause realized responses to differ from the assumed response model. Consequently, the coarse–fine discrepancy measures the update error under the specified model and does not capture every source of mismatch between modeled and realized system behavior. The reliability of a real-world application would therefore depend on the quality of the network and demand data, the calibration of the response model, and the availability of timely measurements. Future validation should use operational data from multiple operating periods and assess the results on held-out conditions.

6. Conclusions

A budget-constrained adaptive method was developed to update locational electricity–carbon signals during sequential demand response. For each candidate macro step, the method compares one coarse response step with two re-cleared half steps, accepts the fine endpoint when the observed discrepancy satisfies the prescribed threshold, and adjusts the next batch size accordingly. This procedure allocates re-clearing effort along the participation path without requiring the operator to specify a fixed number of groups in advance. Under the stated regularity assumptions, the accepted trajectory converges to the continuous ordered-participation path with first-order accuracy as the maximum accepted step decreases.

The results show that collective demand response can make static signals unreliable. At the 1× participation level, price-only response reduced operating cost by 0.789% but increased emissions by 7.83 tCO_2. At 5× participation, the static LMCE predicted an emission reduction of 34.45 tCO_2, whereas only 4.22 tCO_2 was realized after market re-clearing. Across the five tested participation scales, the comparison with budget-feasible fixed groupings did not establish a general accuracy advantage for adaptive batching: the advantage at 1× was resolved relative to the estimated reference uncertainty, the comparison at 2× was marginal, and the rankings at 3×, 5×, and 8× remained unresolved. At 5×, adaptive batching required 2349 SCED solves and 368.65 s, compared with 1941 solves and 308.29 s for the fixed 20-group scheme, while their operating-cost and emission outcomes were nearly identical. The demonstrated value of the method is therefore its ability to select update locations without prior knowledge of a suitable fixed group count, rather than guaranteed accuracy or computational superiority at every operating point.

Several limitations bound these findings. The numerical evaluation uses a modified IEEE 14-bus system and specified model inputs; it has not been validated against real-world operational data and does not establish scalability to larger networks. The participation path assumes that each admitted batch preserves a fixed composition of aggregator types, so the results do not represent arbitrary heterogeneous arrival sequences. The coarse–fine discrepancy is a local update indicator rather than a global error certificate, and the endpoint comparisons depend on a numerical reference path whose estimated remaining error reaches 0.413 MWh. Repeated SCED calculations also impose a computational burden, as illustrated by the higher solve count and runtime of the adaptive scheme at 5× participation.

Future work should validate the framework with calibrated network, market, demand, and aggregator data across multiple operating periods, including held-out conditions. It should also test larger, city-wide networks with alternating-current network constraints, unit commitment, nonlinear emissions, and more detailed storage models. Potential implementation measures include warm-starting and sparse-solver reuse, coordinated zonal decomposition where appropriate, cohort-based representation of large consumer populations, and error thresholds calibrated to system size and operational tolerances. These measures must preserve system-wide feasibility and be evaluated against both endpoint

accuracy and wall-clock deadlines. Further studies should examine heterogeneous participation sequences, response delays, incomplete participation, and whether the required re-clearings can be completed within available SCED budgets.

Author Contributions: Conceptualization, J.X. and L.Z.; methodology, J.X. and Y.Z.; software, Y.Z. and C.G.; validation, C.G., W.H. and N.F.; formal analysis, J.X. and Y.Z.; investigation, W.H. and N.F.; resources, L.Z., W.H. and N.F.; writing—original draft preparation, J.X.; writing—review and editing, all authors; supervision, L.Z.; project administration, J.X. and L.Z. All authors have read and agreed to the published version of the manuscript.

Funding: This work was supported by the State Grid Fujian Electric Power Co.,Ltd. Science and Technology Project Funding under Grant 52130N260009.

Data Availability Statement: The hourly coefficients and construction rules needed to reconstruct the baseline nodal-demand and renewable-availability inputs are provided in Appendix C.

Conflicts of Interest: Authors Jingwei Xue, Linyao Zhang, Yuxi Zheng and Chenhao Guan were employed by State Grid Fujian Economic Research Institute. Authors Weiqiong Huang and Nan Fang were employed by State Grid Zhangzhou Electric Power Supply Company. This study received funding from State Grid Fujian Electric Power Co., Ltd. The funder had no role in the design of the study; in the collection, analyses, or interpretation of data; in the writing of the manuscript; or in the decision to publish the results. The authors declare no other conflicts of interest.

Appendix A. Proof of Proposition 4

For brevity, write $f = f^{\delta_m}$. By the definitions of the coarse and fine endpoints,

$$\Phi_\omega(D) = D + \omega f(D) \tag{A1}$$

and

$$\Psi_\omega(D) = D + \frac{\omega}{2} f(D) + \frac{\omega}{2} f\Big(D + \frac{\omega}{2} f(D)\Big). \tag{A2}$$

Under the assumptions of Proposition 4, the midpoint and both candidate paths remain in the same region on which f is twice continuously differentiable. Taylor's theorem at D therefore gives

$$f\Big(D + \frac{\omega}{2} f(D)\Big) = f(D) + \frac{\omega}{2} J_f(D) f(D) + O(\omega^2). \tag{A3}$$

Substituting this expansion into the fine endpoint yields

$$\Psi_\omega(D) = D + \omega f(D) + \frac{\omega^2}{4} J_f(D) f(D) + O(\omega^3). \tag{A4}$$

Subtracting $\Phi_\omega(D)$ proves Equation (71):

$$\Psi_\omega(D) - \Phi_\omega(D) = \frac{\omega^2}{4} J_{f^{\delta_m}}(D) f^{\delta_m}(D) + O(\omega^3). \tag{A5}$$

Finally, since $e_\omega(D) = \|\Psi_\omega(D) - \Phi_\omega(D)\|_2$ and $|\|a + r\|_2 - \|a\|_2| \le \|r\|_2$, taking norms gives Equation (72):

$$e_\omega(D) = \frac{\omega^2}{4} \left\| J_{f^{\delta_m}}(D) f^{\delta_m}(D) \right\|_2 + O(\omega^3). \tag{A6}$$

The Taylor expansion requires the stated smooth-region condition; this proof does not establish the same asymptotic relation across an active-set boundary.

Appendix B. Proof of Theorem 1

Let $\omega_1, \dots, \omega_G$ be the accepted macro-step fractions, with $\sum_{g=1}^{G} \omega_g = 1$, and set $h = \max_{1 \le g \le G} \omega_g$. Split each accepted macro step into its two implemented half steps. Write $N = 2G$ and define

$$\Delta_{2g-1} = \Delta_{2g} = \frac{\omega_g}{2}, \qquad g = 1, \dots, G. \tag{A7}$$

Let $p_0 = 0$ and $p_j = \sum_{k=1}^{j} \Delta_k$, so that $p_N = 1$. Denote the implemented states on this substep grid by U_j:

$$U_0 = D^{(0)}, \qquad U_{2g-1} = D^{(g)}_{\mathrm{mid}}, \qquad U_{2g} = D^{(g)}. \tag{A8}$$

Equation (53) then gives the exact update performed by the implementation:

$$U_{j+1} = U_j + \Delta_{j+1} f^{\delta_m}(U_j), \qquad j = 0, \dots, N-1. \tag{A9}$$

In particular, $U_N = D^{(G)}$. The auxiliary coarse endpoints $\widehat{D}^{(g)}$ are not states on this accepted grid.

Let $D(p)$ be the continuous path in Equation (51). For one substep, its local truncation error is

$$r_{j+1} = D(p_{j+1}) - D(p_j) - \Delta_{j+1} f^{\delta_m}(D(p_j)). \tag{A10}$$

The Lipschitz and boundedness assumptions imply

$$\|D(p_j + s) - D(p_j)\|_2 \le F_f s \tag{A11}$$

for $0 \le s \le \Delta_{j+1}$. Integrating the difference between $f^{\delta_m}(D(p_j + s))$ and $f^{\delta_m}(D(p_j))$ therefore gives

$$\|r_{j+1}\|_2 \le \frac{L_f F_f}{2} \Delta_{j+1}^2. \tag{A12}$$

Set $E_j = \|U_j - D(p_j)\|_2$. Since $E_0 = 0$, the implemented update and Lipschitz continuity yield

$$E_{j+1} \le (1 + L_f \Delta_{j+1}) E_j + \frac{L_f F_f}{2} \Delta_{j+1}^2. \tag{A13}$$

Every implemented substep satisfies $\Delta_{j+1} \le h/2$. With $a = F_f h/4$, the last term is at most $L_f a \Delta_{j+1}$, and hence

$$E_{j+1} + a \le (1 + L_f \Delta_{j+1})(E_j + a). \tag{A14}$$

Iterating, using $E_0 = 0$ and $\sum_{j=1}^{N} \Delta_j = 1$, we obtain

$$E_N + a \le a \prod_{j=1}^{N} (1 + L_f \Delta_j) \le a e^{L_f}. \tag{A15}$$

Because $U_N = D^{(G)}$ and $p_N = 1$, it follows that

$$\|D^{(G)} - D(1)\|_2 \le \frac{F_f}{4} (e^{L_f} - 1) h \le \frac{L_f F_f}{4} e^{L_f} h = O(h). \tag{A16}$$

The second inequality follows from $e^{L_f} - 1 \le L_f e^{L_f}$ for $L_f \ge 0$ and yields the bound stated in Theorem 1. If $L_f = 0$, the bound is understood by continuity and the endpoint error is zero. Adaptive acceptance changes the substep lengths but not this argument, provided that the theorem's assumptions hold and all participation is allocated.

Appendix C. Numerical Parameters of the Test System and Adaptive Controller

The base network topology, branch electrical parameters, and reference nodal active demands are taken from the IEEE 14-bus case [22]. The hourly demand and renewable-availability profiles are synthetic inputs constructed for method validation.

Hourly nodal demand is calculated as

$$D^0_{i,t} = P^{\text{case14}}_{d,i} \ell_{k(i),t}, \tag{A17}$$

where $P^{\text{case14}}_{d,i}$ is the reference active demand at bus i in the IEEE 14-bus reference case described in [22], and $\ell_{k(i),t}$ is the hourly coefficient for the assigned load type in Table A1. Buses 2, 3, 6, 12, and 13 use the industrial profile; buses 4 and 9 use the commercial profile; and buses 5, 10, 11, and 14 use the residential profile. Buses 1, 7, and 8 have zero baseline demand. The resulting nodal demands are rounded to six decimal places in MW.

Renewable availability is calculated as

$$P^{\text{avail}}_{r,t} = s_{\text{RE}} C_r \text{CF}_{r,t}, \qquad s_{\text{RE}} = 0.65, \tag{A18}$$

where C_r is the installed capacity and $\text{CF}_{r,t}$ is the capacity factor. The wind capacities at buses 3 and 6 are 100 and 80 MW, respectively, and both use the wind profile in Table A1. The photovoltaic capacities at buses 9 and 14 are 80 and 50 MW, respectively, and both use the photovoltaic profile. These rules and coefficients specify the actual 24 h baseline input series used in the simulations.

The installed renewable capacities are 100 and 80 MW for the wind farms at buses 3 and 6, and 80 and 50 MW for the photovoltaic plants at buses 9 and 14, respectively. The renewable-capacity scale is 0.65. The capacity of line L20 (from bus 13 to bus 14) is set to 0.24 times its input rating of 45 MW.

Table A2 reports the generator coefficients used by the dispatch model. The linear production-cost coefficient is the sum of the marginal-cost and variable-operation-cost fields in the input data. The maximum outputs of the generators at buses 1, 2, and 8 are modified to 80, 60, and 20 MW, respectively.

Flexible demand is represented at buses 3, 4, 9, and 14. The corresponding aggregator types are industrial, commercial, commercial, and residential, with baseline shift limits of 0.15, 0.12, 0.12, and 0.10 times the associated hourly demand, respectively. The quadratic discomfort coefficient used in the response model is $\kappa = 20/A$, where A is the participation scale used in the corresponding experiment. The market model uses a quadratic generation cost coefficient of 0.05, a carbon price of 100 CNY/tCO_2, and a carbon-cost pass-through rate of 0.70. The electricity–carbon signal uses a carbon value of 180 CNY/tCO_2.

For the adaptive-controller experiments, the tested error tolerances are 0.50, 1.00, and 2.00 MWh; the principal comparison uses $\tau_D = 2.00$ MWh. The safety factor is $\beta = 0.90$, the minimum macro step in the implementation's participation-scale units is 0.02, and the maximum number of macro steps is 80. On rejection, the step multiplier is clipped to $[0.25, 0.80]$; after acceptance, it is clipped to $[0.60, 2.00]$ and the next trial step cannot exceed the remaining participation. A local error not exceeding 10^{-12} MWh uses the maximum growth multiplier of 2.00. The SCED problems are solved using a dual-simplex algorithm, with feasibility and optimality tolerances of 10^{-7}.

Table A1. Hourly coefficients used to construct the baseline input series. All coefficients are dimensionless.

Hour	Industrial	Commercial	Residential	Wind CF	PV CF
1	0.66	0.48	0.58	0.55	0.00
2	0.63	0.45	0.53	0.58	0.00
3	0.61	0.43	0.50	0.62	0.00
4	0.60	0.42	0.48	0.64	0.00
5	0.61	0.43	0.49	0.61	0.00
6	0.66	0.47	0.55	0.56	0.02
7	0.74	0.55	0.68	0.49	0.10
8	0.84	0.67	0.79	0.43	0.25
9	0.91	0.79	0.76	0.38	0.43
10	0.95	0.88	0.70	0.34	0.61
11	0.97	0.94	0.67	0.31	0.75
12	0.96	0.98	0.65	0.29	0.84
13	0.94	1.00	0.64	0.27	0.88
14	0.95	0.99	0.65	0.28	0.83
15	0.97	0.98	0.68	0.31	0.72
16	0.98	0.97	0.72	0.35	0.56
17	0.97	0.98	0.79	0.41	0.36
18	0.94	1.00	0.90	0.48	0.16
19	0.90	0.96	0.98	0.54	0.04
20	0.84	0.87	1.00	0.59	0.00
21	0.78	0.75	0.96	0.62	0.00
22	0.73	0.65	0.88	0.61	0.00
23	0.70	0.58	0.76	0.59	0.00
24	0.68	0.52	0.66	0.57	0.00

Table A2. Generator parameters used in the modified IEEE 14-bus case.

Generator Bus	Emission Factor (tCO_2/MWh)	Linear Cost (CNY/MWh)	P_g^{max} (MW)
1	0.82	308	80
2	0.88	344	60
3	0.40	450	90
6	0.55	636	80
8	0.00	118	20

Appendix D. Scenario Construction and Uncertainty-Analysis Settings

Renewable forecast errors are generated as multiplicative errors on the forecast wind and photovoltaic outputs. At unit uncertainty scale, the hourly standard deviations are 0.12 and 0.18 of forecast output for wind and photovoltaic generation, respectively. Each renewable type follows an hourly AR(1) process with coefficient 0.75. A common spatial component with weight 0.45 is combined with an independent component for each renewable unit. Realized outputs are clipped to the interval from zero to the scaled installed capacity.

The training set contains 24 scenarios generated with seed 20260827. Twelve equally spaced scenarios from this set are used to estimate the electricity–carbon signal distribution. The scenario-mean signal is the arithmetic mean of these 12 signals. The robust uncertainty band at each hour and bus is the empirical 90th percentile of the absolute deviation from the mean signal plus 5% of the absolute mean signal. The robust objective uses uncertainty weight $\gamma = 0.80$.

The CVaR-based response uses confidence level $\alpha = 0.90$ and risk weight 1.00. Its objective combines expected electricity cost, expected emissions valued at 180 CNY/tCO_2,

the weighted CVaR of scenario-based emission changes, and the quadratic discomfort term. The participation scale for this auxiliary analysis is 3.00.

Out-of-sample performance is evaluated using 30 independently generated scenarios at each renewable-uncertainty scale of 0.50, 1.00, 1.50, and 2.00. The test-scenario random seeds are generated as 20261827, 20261927, 20262027, and 20262127, respectively. Each response schedule is evaluated against the no-response dispatch under the same realized renewable scenario. The uncertainty-analysis optimization problems are solved numerically with computational logging disabled.

References

1. Cabot, C.; Villavicencio, M. The demand-side flexibility in liberalised power market: A review of current market design and objectives. *Renew. Sustain. Energy Rev.* **2024**, *201*, 114643. [CrossRef]
2. Stanelyte, D.; Radziukyniene, N.; Radziukynas, V. Overview of Demand-Response Services: A Review. *Energies* **2022**, *15*, 1659. [CrossRef]
3. Nilges, B.; Haese, A.; Reinert, C.; von der Assen, N. Validity ranges of locational marginal emission factors for the environmental assessment of electric load shifting. *Appl. Energy* **2025**, *380*, 125069. [CrossRef]
4. Wen, L.; Zhou, K.; Feng, W.; Yang, S. Demand Side Management in Smart Grid: A Dynamic-Price-Based Demand Response Model. *IEEE Trans. Eng. Manag.* **2024**, *71*, 1439–1451. [CrossRef]
5. Silva, C.; Faria, P.; Vale, Z.; Terras, J.M.; Albuquerque, S. Rating the participation in Demand Response events with a contextual approach to improve accuracy of aggregated schedule. *Energy Rep.* **2022**, *8*, 8282–8300. [CrossRef]
6. Yang, C.; Liu, J.; Liao, H.; Liang, G.; Zhao, J. An improved carbon emission flow method for the power grid with prosumers. *Energy Rep.* **2023**, *9*, 114–121. [CrossRef]
7. Li, G.; Wang, Q.; Wang, P.; Lin, Y.; Yang, J.; Lu, Z.; Zhang, X.; Jia, D.; Zhao, Z.; Yao, S. Dynamic Measurement of Power Grid Carbon Emission Factors Based on Carbon Emission Flow Theory. *Energies* **2026**, *19*, 950. [CrossRef]
8. Valenzuela, L.F.; Degleris, A.; Gamal, A.E.; Pavone, M.; Rajagopal, R. Dynamic Locational Marginal Emissions via Implicit Differentiation. *IEEE Trans. Power Syst.* **2024**, *39*, 1138–1147. [CrossRef]
9. Sang, L.; Xu, Y.; Sun, H.; Wu, Z.; Wu, Q.; Wu, W. Distribution Locational Marginal Emission for Carbon Alleviation in Distribution Networks: Formulation, Calculation, and Implication. *IEEE Trans. Autom. Sci. Eng.* **2025**, *22*, 15006–15017. [CrossRef]
10. Degleris, A.; Valenzuela, L.F.; Rajagopal, R.; Pavone, M.; Gamal, A.E. Fast Grid Emissions Sensitivities using Parallel Decentralized Implicit Differentiation. In *Proceedings of the 2024 IEEE International Conference on Communications, Control, and Computing Technologies for Smart Grids (SmartGridComm)*; IEEE: New York, NY, USA, 2024; pp. 458–464. [CrossRef]
11. Koebrich, S.; Cofield, J.; McCormick, G.; Saraswat, I.; Steinsultz, N.; Christian, P. Towards objective evaluation of the accuracy of marginal emissions factors. *Renew. Sustain. Energy Rev.* **2025**, *215*, 115508. [CrossRef]
12. Miri, M.; McPherson, M. Demand response programs: Comparing price signals and direct load control. *Energy* **2024**, *288*, 129673. [CrossRef]
13. Salazar, E.J.; Jurado, M.; Samper, M.E. Reinforcement Learning-Based Pricing and Incentive Strategy for Demand Response in Smart Grids. *Energies* **2023**, *16*, 1466. [CrossRef]
14. Qian, T.; Liang, Z.; Shao, C.; Zhang, H.; Hu, Q.; Wu, Z. Offline DRL for Price-Based Demand Response: Learning From Suboptimal Data and Beyond. *IEEE Trans. Smart Grid* **2024**, *15*, 4618–4635. [CrossRef]
15. Mostafaeipour, A.; Bidokhti, A.; Fakhrzad, M.B.; Sadegheih, A.; Zare Mehrjerdi, Y. A new model for the use of renewable electricity to reduce carbon dioxide emissions. *Energy* **2022**, *238*, 121602. [CrossRef]
16. Gordic, D.; Nikolic, J.; Vukasinovic, V.; Josijevic, M.; Aleksic, A.D. Offsetting carbon emissions from household electricity consumption in Europe. *Renew. Sustain. Energy Rev.* **2023**, *175*, 113154. [CrossRef]
17. Yan, N.; Ma, G.; Li, X.; Guerrero, J.M. Low-Carbon Economic Dispatch Method for Integrated Energy System Considering Seasonal Carbon Flow Dynamic Balance. *IEEE Trans. Sustain. Energy* **2023**, *14*, 576–586. [CrossRef]
18. Park, B.; Dong, J.; Liu, B.; Kuruganti, T. Decarbonizing the grid: Utilizing demand-side flexibility for carbon emission reduction through locational marginal emissions in distribution networks. *Appl. Energy* **2023**, *330*, 120303. [CrossRef]
19. Hu, J.; Shi, M.; Dong, Q.; Zhang, X.p.; Jia, Y. Low-carbon Oriented Framework for Large-scale Electric Vehicle Deployment Incorporating Transmission Network Impacts. *IEEE Trans. Ind. Appl.* **2026**, *Early Access*. [CrossRef]
20. Ndrio, M.; Bose, S.; Tong, L.; Guo, Y. Coordinated Transaction Scheduling in Multi-Area Electricity Markets: Equilibrium and Learning. *IEEE Trans. Power Syst.* **2023**, *38*, 996–1008. [CrossRef]

21. Wu, C.; Yang, L.; Lin, C. Multiparametric Programming-Based Coordinated Economic Dispatch of Integrated Electricity and Natural Gas System. *IEEE Syst. J.* **2023**, *17*, 2523–2533. [CrossRef]
22. Zholbaryssov, M.; Domínguez-García, A.D. Safe Data-Driven Secondary Control of Distributed Energy Resources. *IEEE Trans. Power Syst.* **2021**, *36*, 5933–5943. [CrossRef]

Disclaimer/Publisher's Note: The statements, opinions and data contained in all publications are solely those of the individual author(s) and contributor(s) and not of MDPI and/or the editor(s). MDPI and/or the editor(s) disclaim responsibility for any injury to people or property resulting from any ideas, methods, instructions or products referred to in the content.